

Coupling of MoS₂ Excitons with Lattice Phonons and Cavity Vibrational Phonons in Hybrid Nanobeam Cavities

Chenjiang Qian,^{1,*} Viviana Villafañe,¹ Marko M. Petrić,²
 Pedro Soubelet,¹ Andreas V. Stier,¹ and Jonathan J. Finley^{1,†}

¹Walter Schottky Institut and Physik Department,
 Technische Universität München, Am Coulombwall 4, 85748 Garching, Germany
²Walter Schottky Institut and Department of Electrical and Computer Engineering,
 Technische Universität München, Am Coulombwall 4, 85748 Garching, Germany

We report resonant Raman spectroscopy of neutral excitons X^0 and intravalley trions X^- in hBN-encapsulated MoS₂ monolayer embedded in a nanobeam cavity. By temperature tuning the detuning between Raman modes of MoS₂ lattice phonons and X^0/X^- emission peaks, we probe the mutual coupling of excitons, lattice phonons and cavity vibrational phonons. We observe an enhancement of X^0 -induced Raman scattering and a suppression for X^- -induced, and explain our findings as arising from the tripartite exciton-phonon-phonon coupling. The cavity vibrational phonons provide intermediate replica states of X^0 for resonance conditions in the scattering of lattice phonons, thus enhancing the Raman intensity. In contrast, the tripartite coupling involving X^- is found to be much weaker, an observation explained by the geometry-dependent polarity of the electron and hole deformation potentials. Our results indicate that phononic hybridization between lattice and nanomechanical modes plays a key role in the excitonic photophysics and light-matter interaction in 2D-material nanophotonic systems.

Nano-opto-electro-mechanical systems are of strong interest in the study of light-matter interactions since they intentionally couple electronic, optical and vibrational degrees of freedom having vastly different eigenfrequencies [1–4]. Hereby, interband optical response becomes sensitive to the local optical field and the state of motion (phonons) in the nanosystem [5, 6]. Monolayer transition metal dichalcogenides (TMDs) are of particular interest in this context since they (i) can be attached via van der Waals bonding to a wide range of different substrates, and they combine (ii) strong light-matter interactions through excitonic transitions at room temperature with (iii) large photoelastic coupling strengths to the local deformations [7–10]. Recent works on 2D-material nanophotonic cavities report that phonons modulate the light-matter interaction by limiting the exciton mobility [11] and introducing vibronic sublevels [12, 13]. These phonon-mediated effects indicate wide potentials of phononic technology in the cavity QED study.

While these recent works spell out the key role played by phonons in 2D-material nanocavities [11–14], the additional degree of freedom associated with the phononic vibration from cavity nanomechanical modes and the delicate interplay between lattice phonons, nanomechanical modes, excitons, and cavity photons have not been previously elucidated. Indeed, besides the lattice phonons from atomic vibrational modes [15–18], there also exist the phononic vibrational modes of nanocavities [19–22]. The cavity vibrational phonons also introduce deformations and interact with excitons [23, 24]. Therefore, understanding the interplay between different phonons and

their mutual coupling to excitons are the key to further explore and control phonon-mediated processes in light-matter interactions.

In this letter, we reveal the tripartite coupling between excitons, lattice phonons and cavity vibrational phonons in the cavity-MoS₂ system using resonant Raman spectroscopy. We use optimized high-Q nanobeam cavities to embed hBN-encapsulated monolayer MoS₂ [11]. The encapsulation suppresses disorder-induced fluctuations [25–27] and allows clear spectral separation of *pristine* neutral excitons X^0 and intravalley trions X^- . We tune the Raman modes of MoS₂ lattice phonons through the exciton emission energies by the temperature [28]. The $X^0(X^-)$ -phonon coupling strengths in the $X^0(X^-)$ -induced Raman scattering are revealed by the X^0 -Raman and X^- -Raman resonant peaks in the detuning dependent Raman intensity [28–31]. We observe a significant enhancement of X^0 -induced Raman scattering and a suppression for X^- -induced. The enhancement of X^0 -induced scattering is well explained by exciton-phonon-phonon coupling, where the cavity vibrational phonons provide intermediate replica states for resonance conditions in the scattering of lattice phonons. In contrast, the X^- -cavity-phonon coupling is very weak, explained by the near cancellation of electron and hole deformation potentials in the ribbon-shaped MoS₂ monolayers [32]. Thereby, the intermediate state which enhances the Raman intensity does not occur for X^- . The temperature dependence of Raman enhancement reveals that a discrete number of cavity phonons participate in the coupling, further supporting the phononic hybridization between material and nanomechanical degrees of freedom in the quantum system.

Our sample structures are depicted in Fig. 1(a). The hBN/MoS₂/hBN heterostructure is prepared using mechanical exfoliation and viscoelastic dry transfer meth-

* chenjiang.qian@wsi.tum.de

† finley@wsi.tum.de

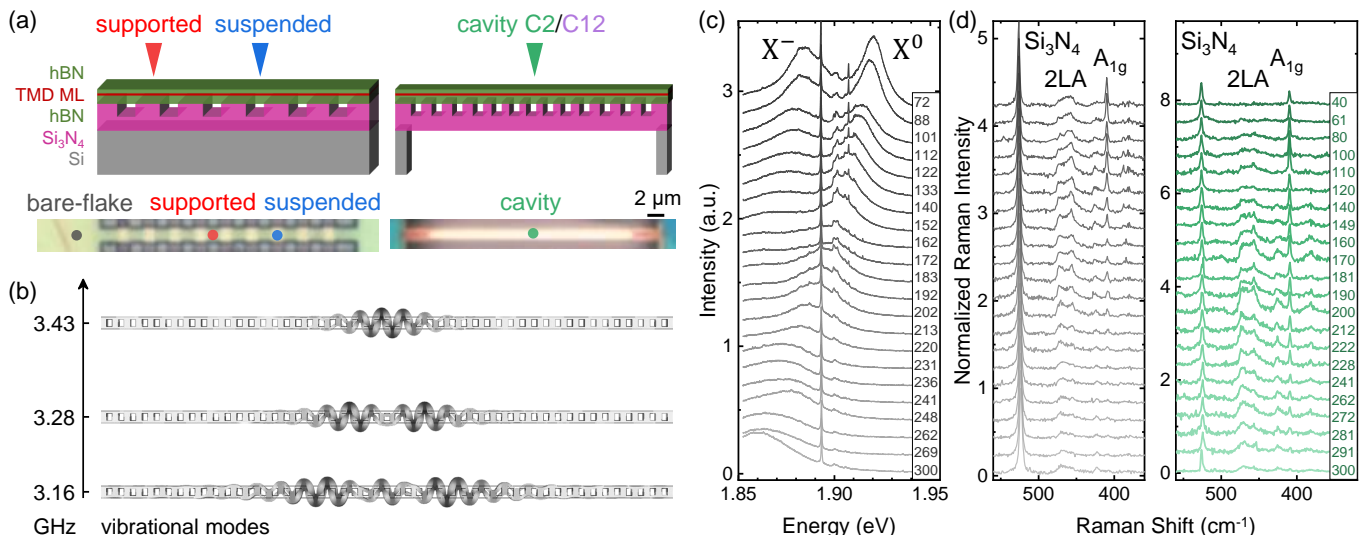


FIG. 1. (a) Schematic of four distinct laser positions for spectroscopy: bare flake off to the side of nanobeam on the planar substrate, supported on Si₃N₄ and suspended on etched Si₃N₄ part of the nanobeam, and the center position of the nanobeam cavity. (b) Calculated vibrational modes of the nanobeam cavity. The MoS₂ deforms primarily along the axis of nanobeam. (c) Temperature-dependent raw spectra recorded from the bare flake showing both Raman and photoluminescence (PL) signals. (d) Raman spectra after subtracting the PL emission baseline recorded from the bare flake (gray) and cavity C2 (green). Intensities are normalized to the Si₃N₄ peak. Temperatures are denoted in Kelvin in the inset box in (c)(d).

ods [11, 33]. The monolayer MoS₂ is encapsulated by the top (bottom) hBN with a thickness around 15 (55) nm, transferred onto a 200 nm thick Si₃N₄ layer on a Si substrate. The sample is patterned into series of photonic crystal nanobeams [11, 34]. We investigate the Raman spectra recorded from four kinds of positions. The first case bare flake corresponds to the region consisting of only hBN-encapsulated MoS₂ on the planar Si₃N₄ substrate. Data recorded from this case are denoted by gray datasets in this work. The second and third cases, denoted by red and blue datasets, correspond to supported and suspended positions in the nanobeam, respectively. Since the photonic crystal trenches in this sample have a periodicity of 2 μm and a lateral size of 1 μm , the laser spot can be precisely and readily positioned on the supported or suspended positions, respectively. These three cases (bare flake, supported, suspended) are control experiments, in contrast to the fourth case cavity corresponding to the center position of high-Q cavities. In this work, we present data recorded from two cavities with the different nanobeam width 520 (420) nm for cavity C2 (C12). The data recorded from cavity C2 (C12) is denoted by green (purple) datasets, respectively. Optical and vibrational modes of the cavity are formed by chirping the photonic crystal periodicity to create photonic and phononic band gap confinement [11, 20]. Typical vibrational modes calculated via fully 3D finite element simulation are presented in Fig. 1(b), and the calculation details are presented in Sec. II in Supplement [35].

The three control experiments, i.e., bare flake, supported and suspended cases are chosen to identify other factors besides the optical and vibrational modes which

might affect the Raman properties in the cavity. For example, in the cavity two types of local static strain are induced in the TMD: tensile strain from Si₃N₄ structures [49, 50] and strain arising from the 2D heterostructure being freely suspended. Effects from the former can be isolated by the supported case, and effects from the latter can be revealed by the suspended case. The reactive ion etching during nanofabrication might also affect the hBN/TMD/hBN heterostructure [51, 52], and if this is the case, the effect on Raman properties can be revealed by both supported and suspended cases.

We implement resonant Raman spectroscopy by varying the lattice temperature to tune the Raman modes of MoS₂ lattice phonons through the X⁰ and X⁻ emission. The excitation cw-laser laser has the wavelength 632 nm with a spot size $\sim 1 \mu\text{m}$ and power $\sim 100 \mu\text{W}$. The excitation conditions produce both exciton emissions and Raman signals superimposed in spectra, as shown in the raw spectra measured from the bare flake in Fig. 1(c). Raman spectra are then extracted by subtracting the emission baseline, and the results from the bare flake and cavity C2 are presented in Fig. 1(d). We observe three dominant Raman modes: the Si₃N₄ phonon (525 cm⁻¹) and two MoS₂ lattice phonons as acoustic phonon 2LA (450 – 480 cm⁻¹) and optical phonon A_{1g} (409 cm⁻¹) [53, 54]. The intensity of 2LA peak in both cases exhibits a clear maximum around the resonance to X⁰, which is a typical resonant Raman phenomenon [28–30]. Meanwhile, differences are observed between cavities and control experiments, e.g., the intensity of 2LA peak at low temperature, indicating the phonons and exciton-phonon couplings are modulated in the cavity.

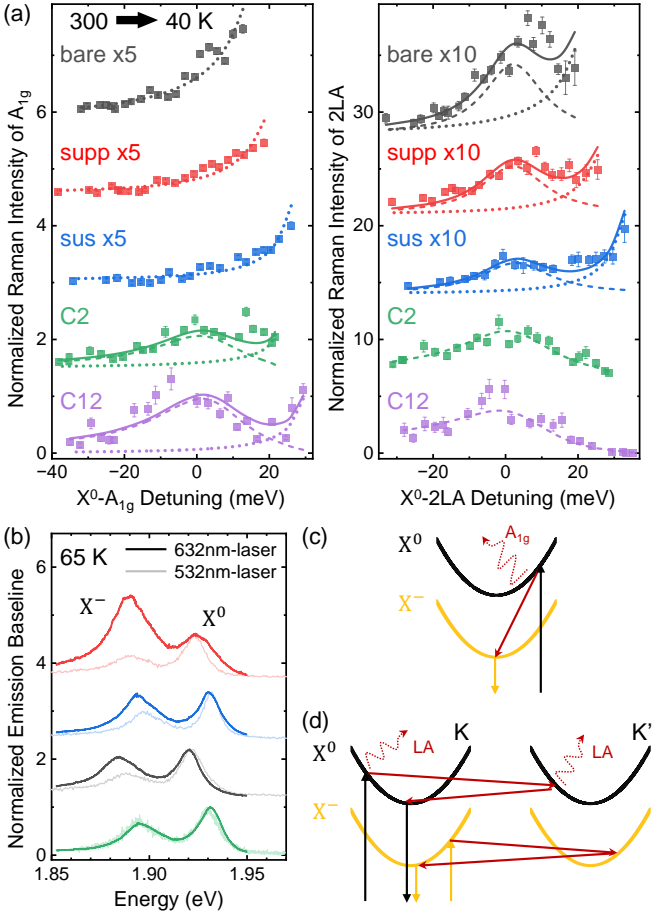


FIG. 2. (a) Normalized Raman intensities of A_{1g} and 2LA. Dashed (dotted) peaks are from the X^0 (X^-)-phonon coupling. In control cases (gray, red, blue) the coupling strength $g_{X,p}$ is constant. In cavities (green, purple), $g_{X-,p}$ is constant and $g_{X^0,p}$ is enhanced with a T^N dependence. (b) Comparisons between exciton emission recorded using 632 nm-laser (dark) and 532 nm-laser (light) at 65 K, normalized by the X^0 peak. (c) Schematic of doubly resonant scattering of A_{1g} around X^- -Raman resonance, which converts X^0 to X^- , thereby enhances the X^- emission in (b) for the three control cases. (d) Schematic of the doubly resonant scattering of 2LA around X^0 (X^-)-Raman resonance.

To further investigate the exciton-phonon couplings, we normalize the Raman intensities by dividing the integrated peak intensity by the Bose factor and the intensity of Si_3N_4 peak [10], i.e.

$$I'_{A_{1g}} = \frac{I_{A_{1g}}/(n_{A_{1g}} + 1)}{I_{\text{SiN}}/(n_{\text{SiN}} + 1)}, I'_{2LA} = \frac{I_{2LA}/(n_{LA} + 1)}{I_{\text{SiN}}/(n_{\text{SiN}} + 1)}$$

where $I_{A_{1g}}$, I_{SiN} and I_{2LA} are peak intensities extracted from Raman spectra. $n_{A_{1g}}$, n_{SiN} , n_{LA} are temperature-dependent Bose distribution factors

$$n_p = \frac{1}{e^{\hbar(\omega_{\text{Laser}} - \omega_p)/(k_B T)} - 1}, p = \{A_{1g}, 2LA, \text{SiN}\}$$

where $\hbar\omega_{\text{Laser}}$ ($\hbar\omega_p$) is the energy of the laser (Raman

mode), k_B is the Boltzmann constant, and T is the temperature. Theoretically, the normalized Raman intensity consists of signals from all possible light-matter intermediate states, according to [55]

$$\sum_m \left| \frac{M_{fm} M_{ep} M_{mi}}{(\omega_m - (i/2)\gamma_m - \omega_{\text{Laser}})(\omega_m - (i/2)\gamma_m - \omega_p)} \right|^2,$$

where i , m and f denote the initial, intermediate and final states, ω_m and γ_m are the energy and lifetime of the intermediate state m , M_{fm} (M_{mi}) is the matrix element of the optical $f \leftarrow m$ ($m \leftarrow i$) transition, and M_{ep} is the matrix element quantifying the exciton-phonon coupling strength. In our measurements, X^0 and X^- are near resonant to the outgoing Raman modes. Thus, the exciton-Raman detuning (outgoing Raman resonance) dominates the detuning-dependent Raman intensities. We thereby fit the normalized Raman intensities using

$$I'_p = \sum_X g_{X,p} R_{X,p}, X = \{X^0, X^-\}, p = \{A_{1g}, 2LA\}$$

$$R_{X,p} = 1/|\omega_X - (i/2)\gamma_X - \omega_p|^2,$$

where $g_{X,p}$ reflects the exciton-phonon coupling strength and $R_{X,p}$ is the exciton-Raman detuning modeled by Fermi's golden rule [28, 30, 31]. The Raman mode energy ω_p are extracted from the Raman spectra. Since the exciton-Raman resonance deforms the exciton emission line shape [29, 56], we extract the exciton energy ω_X and linewidth γ_X from the PL spectra excited by 532 nm-laser (off-resonance, see Sec. IV A in Supplement [35]).

The results of A_{1g} and 2LA measured from the three control cases and two cavities are plotted in Fig. 2(a) as a function of the energy detuning to X^0 . Dashed lines represent the resonance arising from the coupling to X^0 , and dotted lines represent the expected resonance arising from the coupling to X^- , ~ 35 meV detuned from X^0 [29]. In three control cases (gray, red, blue), the coupling strength $g_{X,p}$ is nearly constant [28, 30, 31]. The results reveal that for A_{1g} , only $g_{X^-,A_{1g}}$ has a significant amplitude whilst $g_{X^0,A_{1g}}$ vanishes. For 2LA both $g_{X^0,2LA}$ and $g_{X^-,2LA}$ have finite amplitudes. Another distinctive feature of X^- -Raman resonance is the enhanced ratio of X^-/X^0 emission intensity [29, 56] as clearly observed in three control cases presented in Fig. 2(b), where exciton emission around 65 K recorded using the 632 nm-laser (dark, close to X^- -Raman resonance) are compared with those using the 532 nm-laser (light, off-resonance). This is due to the doubly resonant Raman scattering depicted in Fig. 2(c), where X^0 is converted to X^- by the phonon scattering [56–58]. In contrast to the three control cases, Raman spectra recorded from the cavities exhibit entirely different behaviors that are traced to cavity vibrational phonons. As shown in Fig. 2(a), $g_{X^0,A_{1g}}$ is clearly nonzero in two cavities, evidenced by the resonance (dashed peak) which is in contrast absent in the three control cases. Meanwhile, $g_{X^0,2LA}$ (dashed peak) is enhanced in cavities whilst the amplitude of $g_{X^-,2LA}$

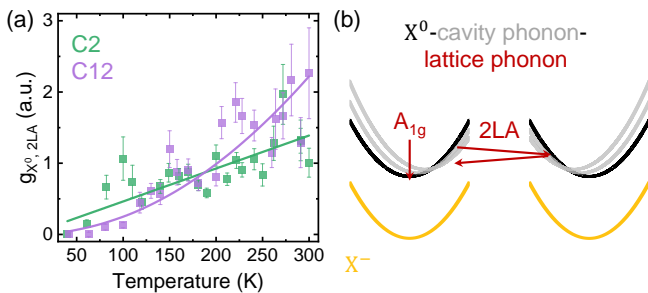


FIG. 3. (a) T^N dependence of $g_{X^0, 2LA}$ in cavities. (b) Schematic depiction of the exciton-phonon-phonon coupling between X^0 (black), cavity phonon (gray replicas) and lattice phonons (dark red arrows).

(dotted peak) vanishes. Therefore, we conclude that X^0 -phonon coupling strengths are enhanced in cavities while X^- -phonon coupling strengths are suppressed. The suppression of $g_{X^-, p}$ is also supported by the exciton emission presented in Fig. 2(b). The X^- emission enhancement [29] arising from X^- -Raman resonance (Fig. 2(c)) is not observed in the cavity.

We note that ingoing Raman resonances have little impact on the measured intensities, since the laser is far detuned from both exciton peaks (X^0 -laser resonance corresponds to 60 meV in X^0 -Raman detuning). Moreover, here A_{1g} and 2LA contain doubly resonant Raman scatterings [30, 31, 56], thereby, the ingoing excitation is not limited to the zone center, as depicted schematically in Fig. 2(c)(d). For the ideal first-order Raman scattering, the ingoing excitation is limited at the zone center, thereby the ingoing resonance between ω_{Laser} and ω_{X^0} play a role in the variation of the Raman intensity. In contrast, in our measurements around the exciton-Raman resonance depicted in Fig. 2(c)(d), only the outgoing section is around the zone center, thereby the outgoing resonances $R_{X, p}$ are expected to dominate the spectral dependencies. Therefore, we fit the detuning-dependent Raman intensities by $R_{X, p}$ as presented in Fig. 2(a). Nevertheless, at this point we emphasize that the conclusions above can be directly obtained from raw data, without making this approximation and quantitative fittings as discussed in Sec. III A in Supplement [35].

Furthermore, the cavity enhanced coupling strengths $g_{X^0, A_{1g}}$ and $g_{X^0, 2LA}$ are found to follow a temperature-dependent power law T^N . This can be seen in Fig. 3(a) that shows $g_{X^0, 2LA} = I'_{2LA}/R_{X^0, 2LA}$ from which we extract $N = 1.14 \pm 0.18$ and 2.21 ± 0.23 for cavity C2 and C12, respectively. The selective enhancement of $g_{X^0, p}$ ($p = \{A_{1g}, 2LA\}$), and the T^N dependence are two key observations in this work, indicating the tripartite coupling between excitons, cavity vibrational phonons and MoS₂ lattice phonons. This exciton-phonon-phonon coupling we envisage is illustrated schematically in Fig. 3(b): cavity vibrational phonons provide additional intermediate states indicated by the gray replicas that can satisfy the resonance conditions in the scattering of MoS₂ lattice

phonons (dark red arrows). The selectivity is due to the vibronic states (gray replicas) that only occur for X^0 but not for X^- . We explain this suggest by the weak X^- -cavity-phonon coupling originating from the geometry-dependent deformation potentials. In cavity vibrational modes, the embedded ribbon-shaped MoS₂ monolayer extends primarily along the nanobeam axis. For such uniaxially strained MoS₂, Cai et al. [32] calculated the width dependent deformation potential for the electrons (D_e) and holes (D_h). D_h was always found to have a magnitude that is approximately twice of D_e [32]. Therefore, the X^- -cavity-phonon coupling strength ($\propto 2D_e - D_h$) is expected to be much smaller than the X^0 -cavity-phonon coupling strength ($\propto D_e - D_h$) [59–61]. This selectivity is further supported by the temperature-dependent linewidth of excitonic PL emission, discussed in SFig. 14 in Supplement [35].

Meanwhile, the T^N dependence is consistent with the Bose occupation of cavity vibrational phonons $n_{cP} = 1/[e^{\hbar\omega_{cP}/(k_B T)} - 1]$. Since the cavity vibrational phonon has low energy (Fig. 1(b)) $\hbar\omega_{cP} \ll k_B T$, the temperature dependent factor of either Stokes ($n_{cP} + 1$) or anti-Stokes (n_{cP}) processes is $\approx k_B T / (\hbar\omega_{cP}) \propto T$. Thereby, N is determined by the number of cavity phonons participating in the tripartite coupling. Additional evidence for the tripartite coupling is observed from the spatial dependence of Raman enhancement and the temperature dependence of Raman linewidth (anharmonicity) [62] as discussed in Sec. III B in Supplement. Similar vibronic sublevel mediated processes have been reported in photonic [12–14, 63] and plasmonic systems [64, 65]. In contrast, other factors do not explain the experimental results. For example, the control experiments in the supported and suspended case show that both two types of static strain without cavity vibrational modes do not result in the selective Raman enhancement. Indeed, the static strain is not proportional to temperature, and thereby, it cannot explain the T^N dependence. The resonant cavity optical mode could of course enhance the Raman intensity by increasing the local optical field for the laser [66, 67] or exciton spontaneous emissions [64, 67, 68]. However, these effects are strongly dependent on the detuning of the cavity optical mode to the laser or excitonic transitions. In our experiments, the excitation laser and Raman modes are far detuned from the cavity optical mode (> 20 meV), and the detuning is nearly temperature independent. The coupling between X^0 and the cavity optical mode is negligible [11], and no dependence on their detuning is observed in Fig. 3(a). Therefore, several pieces of evidence all indicate that the cavity optical mode does not play the major role in determining the observed Raman enhancement.

In summary, we performed spatially resolved Raman spectroscopy to demonstrate how excitons, MoS₂ lattice phonons and cavity vibrational phonons couple to govern the exciton-phonon scattering in 2D-material nanophotonic cavities. The selectivity to the neutral exciton indicates such phononic technology can be applied to con-

trol light-matter interactions based on different electronic transitions (excitonic sorting). Moreover, our results are obtained for thermally excited vibrational modes without external driving [22, 23]. Therefore, our results indicate that the phononic hybridization between lattice and nanomechanical modes has an intrinsic strong impact on excitonic photophysics and light-matter interactions in 2D-material nanophotonic systems.

All authors gratefully acknowledge the German Science Foundation (DFG) for financial support via grants FI 947/8-1, DI 2013/5-1 and SPP-2244, as well as the clusters of excellence MCQST (EXS-2111) and e-conversion (EXS-2089). C. Q. and V. V. gratefully acknowledge the Alexander v. Humboldt foundation for financial support in the framework of their fellowship programme.

C. Q. and V. V. contributed equally to this work.

-
- [1] I. Mahboob, K. Nishiguchi, H. Okamoto, and H. Yamaguchi, Phonon-cavity electromechanics, *Nat. Phys.* **8**, 387 (2012).
- [2] M. Aspelmeyer, T. J. Kippenberg, and F. Marquardt, Cavity optomechanics, *Rev. Mod. Phys.* **86**, 1391 (2014).
- [3] K. E. Khosla, M. R. Vanner, N. Ares, and E. A. Laird, Displacemom Electromechanics: How to Detect Quantum Interference in a Nanomechanical Resonator, *Phys. Rev. X* **8**, 021052 (2018).
- [4] L. Midolo, A. Schliesser, and A. Fiore, Nano-opto-electromechanical systems, *Nat. Nanotechnol.* **13**, 11 (2018).
- [5] Y.-C. Wei, S. F. Wang, Y. Hu, L.-S. Liao, D.-G. Chen, K.-H. Chang, C.-W. Wang, S.-H. Liu, W.-H. Chan, J.-L. Liao, W.-Y. Hung, T.-H. Wang, P.-T. Chen, H.-F. Hsu, Y. Chi, and P.-T. Chou, Overcoming the energy gap law in near-infrared OLEDs by exciton-vibration decoupling, *Nat. Photonics* **14**, 570 (2020).
- [6] T. Zhang, H. Wang, X. Xia, N. Yan, X. Sha, J. Huang, K. Watanabe, T. Taniguchi, M. Zhu, L. Wang, J. Gao, X. Liang, C. Qin, L. Xiao, D. Sun, J. Zhang, Z. Han, and X. Li, A monolithically sculpted van der Waals nano-opto-electro-mechanical coupler, *Light: Sci. Appl.* **11**, 48 (2022).
- [7] M. Ghorbani-Asl, N. Zibouche, M. Wahiduzzaman, A. F. Oliveira, A. Kuc, and T. Heine, Electromechanics in MoS₂ and WS₂: nanotubes vs. monolayers, *Sci. Rep.* **3**, 2961 (2013).
- [8] B. Miller, J. Lindlau, M. Bommert, A. Neumann, H. Yamaguchi, A. Holleitner, A. Högele, and U. Wurstbauer, Tuning the Fröhlich exciton-phonon scattering in monolayer MoS₂, *Nat. Commun.* **10**, 807 (2019).
- [9] N. Morell, A. Reserbat-Plantey, I. Tsioutsios, K. G. Schädler, F. Dubin, F. H. L. Koppens, and A. Bachtold, High Quality Factor Mechanical Resonators Based on WSe₂ Monolayers, *Nano Lett.* **16**, 5102 (2016).
- [10] P. Soubelet, A. A. Reynoso, A. Fainstein, K. Nogajewski, M. Potemski, C. Faugeras, and A. E. Bruchhausen, The lifetime of interlayer breathing modes of few-layer 2H-MoSe₂ membranes, *Nanoscale* **11**, 10446 (2019).
- [11] C. Qian, V. Villafañe, P. Soubelet, A. Hötger, T. Taniguchi, K. Watanabe, N. P. Wilson, A. V. Stier, A. W. Holleitner, and J. J. Finley, Nonlocal Exciton-Photon Interactions in Hybrid High-*Q* Beam Nanocavities with Encapsulated MoS₂ Monolayers, *Phys. Rev. Lett.* **128**, 237403 (2022).
- [12] S. Latini, U. De Giovannini, E. J. Sie, N. Gedik, H. Hübener, and A. Rubio, Phonoritons as Hybridized Exciton-Photon-Phonon Excitations in a Monolayer *h*-BN Optical Cavity, *Phys. Rev. Lett.* **126**, 227401 (2021).
- [13] D. Li, H. Shan, C. Rupprecht, H. Knopf, K. Watanabe, T. Taniguchi, Y. Qin, S. Tongay, M. Nuß, S. Schröder, F. Eilenberger, S. Höfling, C. Schneider, and T. Brixner, Hybridized Exciton-Photon-Phonon States in a Transition Metal Dichalcogenide van der Waals Heterostructure Microcavity, *Phys. Rev. Lett.* **128**, 087401 (2022).
- [14] D. Rosser, T. Fryett, A. Ryou, A. Saxena, and A. Majumdar, Exciton-phonon interactions in nanocavity-integrated monolayer transition metal dichalcogenides, *npj 2D Mater. Appl.* **4**, 20 (2020).
- [15] M. Selig, G. Berghäuser, A. Raja, P. Nagler, C. Schüller, T. F. Heinz, T. Korn, A. Chernikov, E. Malic, and A. Knorr, Excitonic linewidth and coherence lifetime in monolayer transition metal dichalcogenides, *Nat. Commun.* **7**, 13279 (2016).
- [16] P. Dey, J. Paul, Z. Wang, C. E. Stevens, C. Liu, A. H. Romero, J. Shan, D. J. Hilton, and D. Karaickaj, Optical Coherence in Atomic-Monolayer Transition-Metal Dichalcogenides Limited by Electron-Phonon Interactions, *Phys. Rev. Lett.* **116**, 127402 (2016).
- [17] M. Titze, B. Li, X. Zhang, P. M. Ajayan, and H. Li, Intrinsic coherence time of trions in monolayer MoSe₂ measured via two-dimensional coherent spectroscopy, *Phys. Rev. Mater.* **2**, 054001 (2018).
- [18] G. Gupta and K. Majumdar, Fundamental exciton linewidth broadening in monolayer transition metal dichalcogenides, *Phys. Rev. B* **99**, 085412 (2019).
- [19] M. Eichenfield, R. Camacho, J. Chan, K. J. Vahala, and O. Painter, A picogram- and nanometre-scale photonic-crystal optomechanical cavity, *Nature* **459**, 550 (2009).
- [20] M. Eichenfield, J. Chan, R. M. Camacho, K. J. Vahala, and O. Painter, Optomechanical crystals, *Nature* **462**, 78 (2009).
- [21] M. K. Zhalutdinov, J. T. Robinson, J. J. Fonseca, S. W. LaGasse, T. Pandey, L. R. Lindsay, T. L. Reinecke, D. M. Photiadis, J. C. Culbertson, C. D. Cress, and B. H. Houston, Acoustic cavities in 2D heterostructures, *Nat. Commun.* **12**, 3267 (2021).
- [22] H. Xie, S. Jiang, D. A. Rhodes, J. C. Hone, J. Shan, and K. F. Mak, Tunable Exciton-Optomechanical Coupling in Suspended Monolayer MoSe₂, *Nano Lett.* **21**, 2538 (2021).
- [23] M. Montinaro, G. Wüst, M. Munsch, Y. Fontana, E. Russo-Averchi, M. Heiss, A. Fontcuberta i Morral, R. J. Warburton, and M. Poggio, Quantum Dot Optomechanics in a Fully Self-Assembled Nanowire, *Nano Lett.* **14**, 4454 (2014).
- [24] J. C. H. Chen, Y. Sato, R. Kosaka, M. Hashisaka, K. Muraki, and T. Fujisawa, Enhanced electron-phonon coupling for a semiconductor charge qubit in a surface phonon cavity, *Sci. Rep.* **5**, 15176 (2015).
- [25] F. Cadiz, E. Courtade, C. Robert, G. Wang, Y. Shen, H. Cai, T. Taniguchi, K. Watanabe, H. Carrere, D. La-

- garde, M. Manca, T. Amand, P. Renucci, S. Tongay, X. Marie, and B. Urbaszek, Excitonic Linewidth Approaching the Homogeneous Limit in MoS₂-Based van der Waals Heterostructures, *Phys. Rev. X* **7**, 021026 (2017).
- [26] J. Wierzbowski, J. Klein, F. Sigger, C. Straubinger, M. Kremser, T. Taniguchi, K. Watanabe, U. Wurstbauer, A. W. Holleitner, M. Kaniber, K. Müller, and J. J. Finley, Direct exciton emission from atomically thin transition metal dichalcogenide heterostructures near the lifetime limit, *Sci. Rep.* **7**, 12383 (2017).
- [27] A. Raja, L. Waldecker, J. Zipfel, Y. Cho, S. Brem, J. D. Ziegler, M. Kulig, T. Taniguchi, K. Watanabe, E. Malic, T. F. Heinz, T. C. Berkelbach, and A. Chernikov, Dielectric disorder in two-dimensional materials, *Nat. Nanotechnol.* **14**, 832 (2019).
- [28] J.-H. Fan, P. Gao, A.-M. Zhang, B.-R. Zhu, H.-L. Zeng, X.-D. Cui, R. He, and Q.-M. Zhang, Resonance Raman scattering in bulk 2H-MX₂ (M=Mo, W; X=S, Se) and monolayer MoS₂, *J. Appl. Phys.* **115**, 053527 (2014).
- [29] M. R. Molas, K. Nogajewski, M. Potemski, and A. Babiński, Raman scattering excitation spectroscopy of monolayer WS₂, *Sci. Rep.* **7**, 5036 (2017).
- [30] B. R. Carvalho, Y. Wang, S. Mignuzzi, D. Roy, M. Terrones, C. Fantini, V. H. Crespi, L. M. Malard, and M. A. Pimenta, Intervalley scattering by acoustic phonons in two-dimensional MoS₂ revealed by double-resonance Raman spectroscopy, *Nat. Commun.* **8**, 14670 (2017).
- [31] R. N. Gontijo, G. C. Resende, C. Fantini, and B. R. Carvalho, Double resonance Raman scattering process in 2D materials, *J. Mater. Res.* **34**, 1976–1992 (2019).
- [32] Y. Cai, G. Zhang, and Y.-W. Zhang, Polarity-Reversed Robust Carrier Mobility in Monolayer MoS₂ Nanoribbons, *J. Am. Chem. Soc.* **136**, 6269 (2014).
- [33] F. Pizzocchero, L. Gammelgaard, B. S. Jessen, J. M. Caridad, L. Wang, J. Hone, P. Bøggild, and T. J. Booth, The hot pick-up technique for batch assembly of van der Waals heterostructures, *Nat. Commun.* **7**, 11894 (2016).
- [34] C. Qian, V. Villafañe, M. Schalk, G. V. Astakhov, U. Kentsch, M. Helm, P. Soubelet, N. P. Wilson, R. Rizzato, S. Mohr, A. W. Holleitner, D. B. Bucher, A. V. Stier, and J. J. Finley, Unveiling the Zero-Phonon Line of the Boron Vacancy Center by Cavity-Enhanced Emission, *Nano Lett.* **22**, 5137 (2022).
- [35] See Supplementary Information for methods, additional Raman results, and supporting evidence from PL spectroscopy, which includes Refs. [36–48].
- [36] Z. Huang, A. Alharbi, W. Mayer, E. Cuniberto, T. Taniguchi, K. Watanabe, J. Shabani, and D. Shahrjerdi, Versatile construction of van der Waals heterostructures using a dual-function polymeric film, *Nat. Commun.* **11**, 3029 (2020).
- [37] M. He, P. Rivera, D. Van Tuan, N. P. Wilson, M. Yang, T. Taniguchi, K. Watanabe, J. Yan, D. G. Mandrus, H. Yu, H. Dery, W. Yao, and X. Xu, Valley phonons and exciton complexes in a monolayer semiconductor, *Nat. Commun.* **11**, 618 (2020).
- [38] Y. Yu, J. Dang, C. Qian, S. Sun, K. Peng, X. Xie, S. Wu, F. Song, J. Yang, S. Xiao, L. Yang, Y. Wang, X. Shan, M. A. Rafiq, B.-B. Li, and X. Xu, Many-body effect of mesoscopic localized states in MoS₂ monolayer, *Phys. Rev. Mater.* **3**, 051001 (2019).
- [39] J. Klein, M. Florian, A. Hötger, A. Steinhoff, A. Delhomme, T. Taniguchi, K. Watanabe, F. Jahnke, A. W. Holleitner, M. Potemski, C. Faugeras, A. V. Stier, and J. J. Finley, Trions in MoS₂ are quantum superpositions of intra- and intervalley spin states, *Phys. Rev. B* **105**, L041302 (2022).
- [40] S. Thomas, K. M. Ajith, S. Chandra, and M. C. Valsakumar, Temperature dependent structural properties and bending rigidity of pristine and defective hexagonal boron nitride, *J. Phys.: Condens. Matter* **27**, 315302 (2015).
- [41] G. Berghäuser, P. Steinleitner, P. Merkl, R. Huber, A. Knorr, and E. Malic, Mapping of the dark exciton landscape in transition metal dichalcogenides, *Phys. Rev. B* **98**, 020301 (2018).
- [42] J. Krustok, R. Kaupmees, R. Jaaniso, V. Kiisk, I. Sildos, B. Li, and Y. Gong, Local strain-induced band gap fluctuations and exciton localization in aged WS₂ monolayers, *AIP Advances* **7**, 065005 (2017).
- [43] Y. Hu, F. Zhang, M. Titze, B. Deng, H. Li, and G. J. Cheng, Straining effects in MoS₂ monolayer on nanostructured substrates: temperature-dependent photoluminescence and exciton dynamics, *Nanoscale* **10**, 5717 (2018).
- [44] Z. Khatibi, M. Feierabend, M. Selig, S. Brem, C. Linderälrv, P. Erhart, and E. Malic, Impact of strain on the excitonic linewidth in transition metal dichalcogenides, *2D Mater.* **6**, 015015 (2018).
- [45] F. Song, C. Qian, Y. Wang, F. Zhang, K. Peng, S. Wu, X. Xie, J. Yang, S. Sun, Y. Yu, J. Dang, S. Xiao, L. Yang, K. Jin, H. Zhong, and X. Xu, Hot Polarons with Trapped Excitons and Octahedra-Twist Phonons in CH₃NH₃PbBr₃ Hybrid Perovskite Nanowires, *Laser Photonics Rev.* **14**, 1900267 (2020).
- [46] X. Du, G. Blugan, T. Künniger, S. S. Lee, L. Vladislavova, and S. J. Ferguson, Non-linear mechanical properties and dynamic response of silicon nitride bioceramic, *Ceram. Int.* **47**, 33525 (2021).
- [47] H. Mathieu, P. Merle, E. L. Ameziane, B. Archilla, J. Camassel, and G. Poiblaud, Deformation potentials of the direct and indirect absorption edges of GaP, *Phys. Rev. B* **19**, 2209 (1979).
- [48] R. Singh, A. Sarkar, C. Guria, R. J. Nicholl, S. Chakraborty, K. I. Bolotin, and S. Ghosh, Giant Tunable Mechanical Nonlinearity in Graphene-Silicon Nitride Hybrid Resonator, *Nano Lett.* **20**, 4659 (2020).
- [49] D. Hoch, X. Yao, and M. Poot, Geometric Tuning of Stress in Predisplaced Silicon Nitride Resonators, *Nano Lett.* **22**, 4013 (2022).
- [50] Y. Chai, S. Su, D. Yan, M. Ozkan, R. Lake, and C. S. Ozkan, Strain Gated Bilayer Molybdenum Disulfide Field Effect Transistor with Edge Contacts, *Sci. Rep.* **7**, 41593 (2017).
- [51] S. Kim, J. E. Fröch, J. Christian, M. Straw, J. Bishop, D. Totonjian, K. Watanabe, T. Taniguchi, M. Toth, and I. Aharonovich, Photonic crystal cavities from hexagonal boron nitride, *Nat. Commun.* **9**, 2623 (2018).
- [52] J. E. Fröch, Y. Hwang, S. Kim, I. Aharonovich, and M. Toth, Photonic Nanostructures from Hexagonal Boron Nitride, *Adv. Opt. Mater.* **7**, 1801344 (2019).
- [53] R. Saito, Y. Tatsumi, S. Huang, X. Ling, and M. S. Dresselhaus, Raman spectroscopy of transition metal dichalcogenides, *J. Phys.: Condens. Matter* **28**, 353002 (2016).
- [54] A. Molina-Sánchez and L. Wirtz, Phonons in single-layer and few-layer MoS₂ and WS₂, *Phys. Rev. B* **84**, 155413

- (2011).
- [55] Quantum Description of Raman Scattering, in *Raman Spectroscopy in Graphene Related Systems* (John Wiley & Sons, Ltd, 2011) Chap. 5, pp. 103–119.
 - [56] A. M. Jones, H. Yu, J. R. Schaibley, J. Yan, D. G. Mandrus, T. Taniguchi, K. Watanabe, H. Dery, W. Yao, and X. Xu, Excitonic luminescence upconversion in a two-dimensional semiconductor, *Nat. Phys.* **12**, 323 (2016).
 - [57] D. Van Tuan, A. M. Jones, M. Yang, X. Xu, and H. Dery, Virtual Trions in the Photoluminescence of Monolayer Transition-Metal Dichalcogenides, *Phys. Rev. Lett.* **122**, 217401 (2019).
 - [58] S. Ayari, S. Jaziri, R. Ferreira, and G. Bastard, Phonon-assisted exciton/trion conversion efficiency in transition metal dichalcogenides, *Phys. Rev. B* **102**, 125410 (2020).
 - [59] S. Helmrich, A. W. Achtstein, H. Ahmad, M. Kunz, B. Herzog, O. Schoeps, U. Woggon, and N. Owschimikow, High phonon-limited mobility of charged and neutral excitons in mono- and bilayer MoTe₂ (2020), [arXiv:2004.14202](https://arxiv.org/abs/2004.14202).
 - [60] L. Besombes, K. Kheng, L. Marsal, and H. Mariette, Acoustic phonon broadening mechanism in single quantum dot emission, *Phys. Rev. B* **63**, 155307 (2001).
 - [61] M. T. Portella-Oberli, J. Berney, L. Kappei, F. Morier-Genoud, J. Szczytko, and B. Deveaud-Plédran, Dynamics of Trion Formation in In_xGa_{1-x}As Quantum Wells, *Phys. Rev. Lett.* **102**, 096402 (2009).
 - [62] H.-N. Liu, X. Cong, M.-L. Lin, and P.-H. Tan, The intrinsic temperature-dependent Raman spectra of graphite in the temperature range from 4K to 1000K, *Carbon* **152**, 451 (2019).
 - [63] A. Rundquist, A. Majumdar, and J. Vučković, Off-resonant coupling between a single quantum dot and a nanobeam photonic crystal cavity, *Appl. Phys. Lett.* **99**, 251907 (2011).
 - [64] T. c. v. Neuman, R. Esteban, G. Giedke, M. K. Schmidt, and J. Aizpurua, Quantum description of surface-enhanced resonant Raman scattering within a hybrid-optomechanical model, *Phys. Rev. A* **100**, 043422 (2019).
 - [65] E. C. Le Ru and P. G. Etchegoin, Vibrational pumping and heating under SERS conditions: fact or myth?, *Faraday Discuss.* **132**, 63 (2006).
 - [66] R. Salter, J. Chu, and M. Hippler, Cavity-enhanced Raman spectroscopy with optical feedback cw diode lasers for gas phase analysis and spectroscopy, *Analyst* **137**, 4669 (2012).
 - [67] P. Wang, W. Chen, F. Wan, J. Wang, and J. Hu, A review of cavity-enhanced Raman spectroscopy as a gas sensing method, *Appl. Spectrosc. Rev.* **55**, 393 (2020).
 - [68] I. Irfan, S. Golovynskyi, M. Bosi, L. Seravalli, O. A. Yeshchenko, B. Xue, D. Dong, Y. Lin, R. Qiu, B. Li, and J. Qu, Enhancement of Raman Scattering and Exciton/Trion Photoluminescence of Monolayer and Few-Layer MoS₂ by Ag Nanoprisms and Nanoparticles: Shape and Size Effects, *J. Phys. Chem. C* **125**, 4119 (2021).

SUPPLEMENTARY INFORMATION

I. SETUP AND METHODS

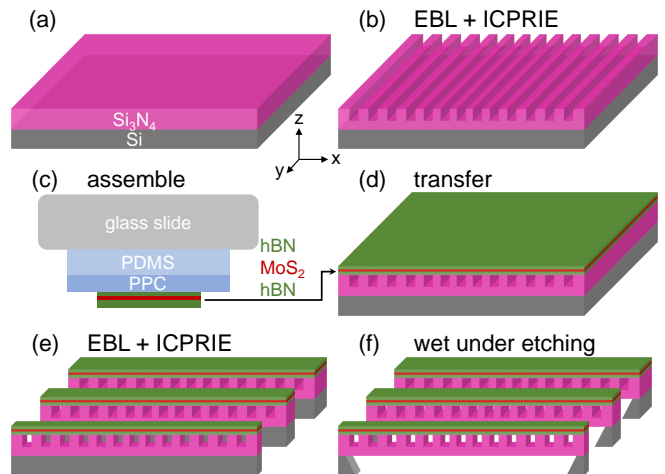
A. Sample Fabrication

The fabrication processes are schematically depicted in SFig. 1. Firstly, as shown in SFig. 1(a) we prepare and clean the $\text{Si}_3\text{N}_4/\text{Si}$ substrate which is from Active Business Company GmbH. The Si_3N_4 is grown by low pressure chemical vapor deposition (LPCVD) and has the thickness of 200 nm. Then we use e-beam lithography (EBL) and inductively coupled plasma reactive ion etching (ICPRIE) to etch the periodic nanoscale trenches in Si_3N_4 . The EBL machine is eLINE from Raith GmbH, and the ebeam resist is AR-P 6200 from Allresist GmbH. We use e-beam at 30 kV with the dose $150 \mu\text{C}/\text{cm}^2$ to pattern the resist with the thickness of 270 nm in this step. The ICPRIE machine is PlasmaPro 80 from Oxford Instruments. We use SF_6 and C_4F_8 with ratio 3:2, pressure 13.5 mTorr, HF power 15 W and ICP power 220 W for ICPRIE. After the first nanofabrication, we prepare and transfer the hBN/MoS₂/hBN heterostructure on top of the pre-etched Si_3N_4 as shown in SFig. 1(c)(d). The bulk hBN and MoS₂ we use for exfoliation are from HQ Graphene. We use the PVA-assisted method to exfoliate huge hBN and MoS₂ flakes [36] and use PPC stamp for the viscoelastic dry transfer [33]. The stacking and transfer is implemented in a home-built machine. Finally, we use the second EBL and ICPRIE to divide the nanobeams as shown in SFig. 1(e) following by the wet etching to remove the bottom Si as shown in SFig. 1(f). In the second EBL, we use the same voltage but the dose $125 \mu\text{C}/\text{cm}^2$ for the resist with the thickness of 480 nm. The gases and parameters in the second ICPRIE are same to the first in SFig. 1(b). We use 25% TMAH solution for the wet under etching in SFig. 1(f).

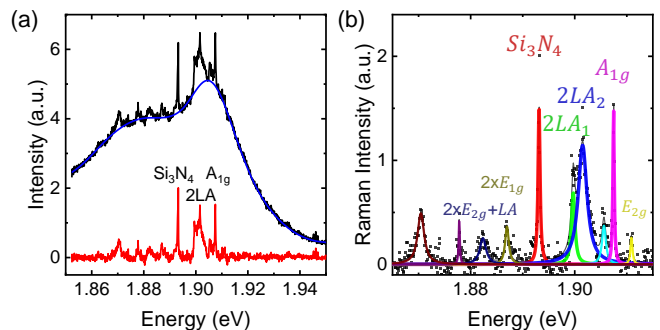
B. Raman Measurement

Raman spectra in this work are measured by a confocal micro-Raman system. The excitation cw-laser has the wavelength of 632 nm. The laser is focused by the objective with a magnification of 100 and a NA of 0.75 into a spot size $\sim 1 \mu\text{m}^2$. The temperature of sample is controlled by the liquid helium flow and heater. The sample position is controlled by a three-dimensional xyz nanopositioner. The signal is collected by a matrix array Si CCD detector in the spectrometer with a focal length of 0.55 m and a grating of 1200 grooves per mm.

As shown in Fig. 1(c), the resonant Raman spectroscopy produce both exciton emissions and Raman signals superimposed in spectra. We present the methods for the subtraction and fitting in SFig. 2. The black line in SFig. 2(a) is the raw data collected by the spectrometer. The minor narrow peaks are from Raman sig-

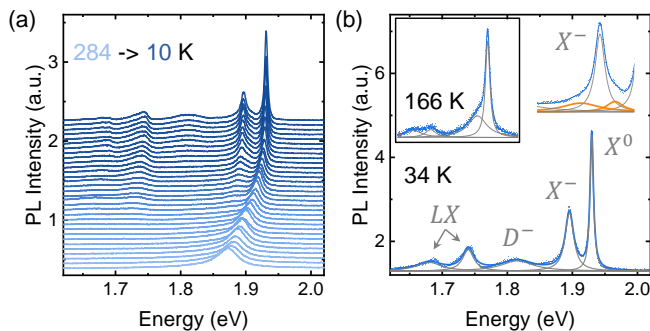


SFig. 1. Design and fabrication of the sample [11]. (a) $\text{Si}_3\text{N}_4/\text{Si}$ substrate. (b) EBL and ICPRIE to fabricate periodic nanoscale trenches. (c) Viscoelastic method to assemble the hBN/MoS₂/hBN heterostructure. (d) Transfer the heterostructure on top of the pre-etched Si_3N_4 . (e) Second EBL and ICPRIE to divide the nanobeams. (f) Wet etching to remove the bottom Si.



SFig. 2. Subtraction and fitting of Raman spectra. (a) One example of the raw data (black) and the corresponding Raman spectrum (red) after subtracting the emission baseline (blue). (b) Multi-Lorentz fitting. The intensity of 2LA discussed in this work is the sum of two peaks (blue and green).

nals, and the broad peaks are from the emission of X^0 and X^- . We sketch the emission baseline based on the feet of minor (Raman) peaks as the blue line. Then the Raman spectra are extracted by subtracting the emission baseline from the raw data, denoted by the red line in SFig. 2(a). Such subtraction method is widely applied in resonant Raman spectroscopy [29]. We then fit the Raman spectra by multi Lorentz peaks as shown in SFig. 2(b). Besides A_{1g} and 2LA, we also observe other Raman peaks. The known Raman peaks are labelled in SFig. 2(b). However, other peaks besides A_{1g} and 2LA are too weak to distinguish when they are strongly detuned to X^0 and X^- . Therefore, we mainly focus on A_{1g} and 2LA in this work.



SFig. 3. (a) Temperature-dependent PL spectra measured in the suspended case. (b) Multi-Lorentz fittings of the PL spectra at 34 and 166 K as examples. PL peaks from neutral exciton X^0 , intravalley trion X^- , dark trion D^- and localized excitons LX (two peaks) are observed [37, 38].

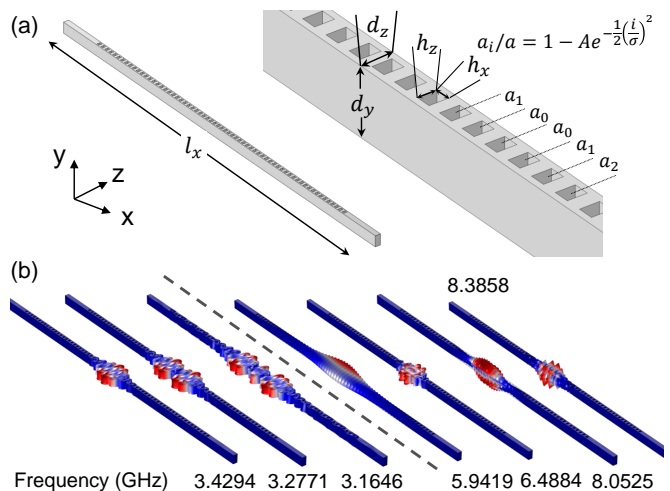
C. PL Measurement

We also study the exciton-phonon coupling using PL spectroscopy. The confocal micro-PL setup is generally same to the micro-Raman setup, but with the excitation cw-laser at 532 nm wavelength. The excitation laser has the spot size $\sim 1 \mu\text{m}$ and the power $\sim 30 \mu\text{W}$. In this case, the Raman modes are strongly detuned from the exciton emissions. The temperature T is similarly controlled by the liquid helium flow and heater. We collect the exciton emission spectra by the spectrometer. Typical temperature-dependent PL spectra measured from the suspended case are presented in SFig. 3(a). We use multi Lorentz fittings to extract the properties of exciton emission peaks including neutral exciton X^0 , intravalley trion X^- , dark trion D^- and localized excitons LX (two peaks) [37, 38] as presented in SFig. 3(b).

However, at high temperature $T > 150 \text{ K}$, the X^- and D^- peak merges such as shown by the spectra at 166 K in SFig. 3(b) inset. As a result, the fitting accuracy of X^- linewidth γ_{X^-} at high T is limited. Moreover, trion emission in monolayer MoS_2 has fine structures. Besides the major emission peak from intravalley singlet trion X^- , there are also minor peaks from intervalley singlet trion, intervalley triplet trion and many-body states [39]. As an alternative fitting method, these minor trion peaks can be extracted at low T , such as shown by the orange peaks in SFig. 3(b). In this work, we extract γ_{X^-} by the fitting without the minor trion peaks. Differences between the two fitting methods (with or without minor trion peaks) are added to the uncertainties of γ_{X^-} .

II. CALCULATION OF CAVITY MODES

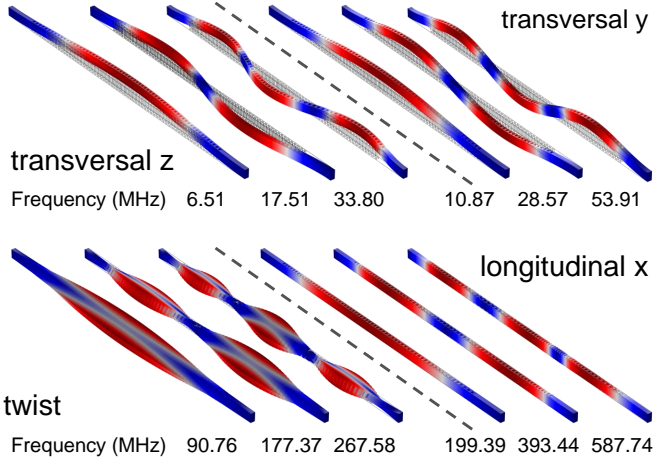
3D finite element method (FEM) method is used to calculate the phononic modes of cavity. Detailed parameters of cavity structure are denoted in SFig. 4(a). The whole nanobeam has the length $l_x = 20 \mu\text{m}$ and depth $d_z = 250 \text{ nm}$. The width is $d_y = 500 \text{ nm}$ in the calcu-



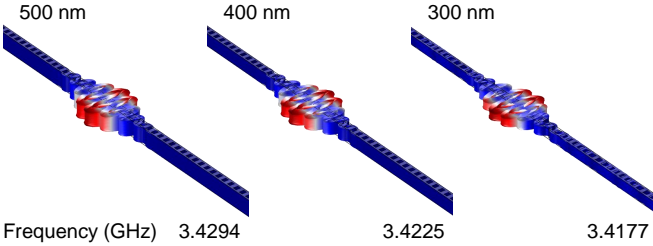
SFig. 4. (a) Cavity structure [11]. (b) Typical confined vibrational modes calculated by FEM method. The first three modes are already plotted in Fig. 1(b).

lation but varies between $d_y = 300 - 530 \text{ nm}$ in experiments. Nanoscale trenches have length $h_x = 120 \text{ nm}$ and depth $h_z = 150 \text{ nm}$, and follow a Gaussian distribution in spatial with the separation between trenches $a_i/a = 1 - A \cdot \exp(-i^2/(2\sigma^2))$. $a = 250 \text{ nm}$ is the lattice constant and $A = 0.1, \sigma = 4$ define the smoothly varying photonic and phononic confinement. The photonic modes have been reported previously [11]. The calculation results of confined phononic (vibrational) modes are presented in SFig. 4(b). As shown, the frequency of confined vibrational modes is $\sim \text{GHz}$. The mode frequency and distribution are consistent to similar structures reported in previous works [2, 19, 20]. Since the phonon energy $\hbar\omega_{cP} \ll k_B T$, the Bose factor of the cavity vibrational phonons $n_{cP} = 1/[e^{\hbar\omega_{cP}/(k_B T)} - 1] \approx k_B T/(\hbar\omega_{cP})$ is proportional to the temperature T . We note that since the optical and mechanical properties of hBN are not well studied yet and strongly depend on the material quality such as the defect concentration [40], we set all material to Si_3N_4 in the calculation. This might introduce inaccuracy in the calculated eigenfrequencies, but the order of magnitudes $\sim \text{GHz}$ should be correct. Even the actual frequency of phononic modes is two order of magnitude larger e.g. 300 GHz, in our measurement range $T > 50 \text{ K}$ we have $\hbar\omega_{cP}/(k_B T) < 0.29$ thus the temperature dependence of the Bose factor is still approximately linear.

In addition, the nanobeam cavity also supports the vibrational modes of the whole nanobeam as presented in SFig. 5. The beam vibrational modes have the frequency $\sim \text{MHz}$, even lower than the confined vibrational modes. Meanwhile, the nanobeam width d_y rarely affects the cavity mode profile and slightly modifies the mode frequency, as presented in SFig. 6. The key point is that the Bose factor of all these cavity modes is $\propto T$. This linear dependence provides the explanation for the T^N dependence in the Raman enhancement.



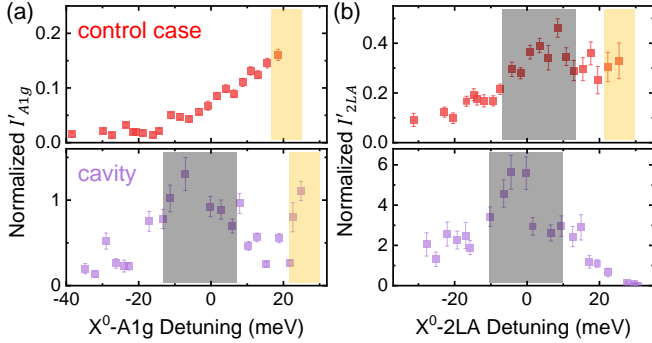
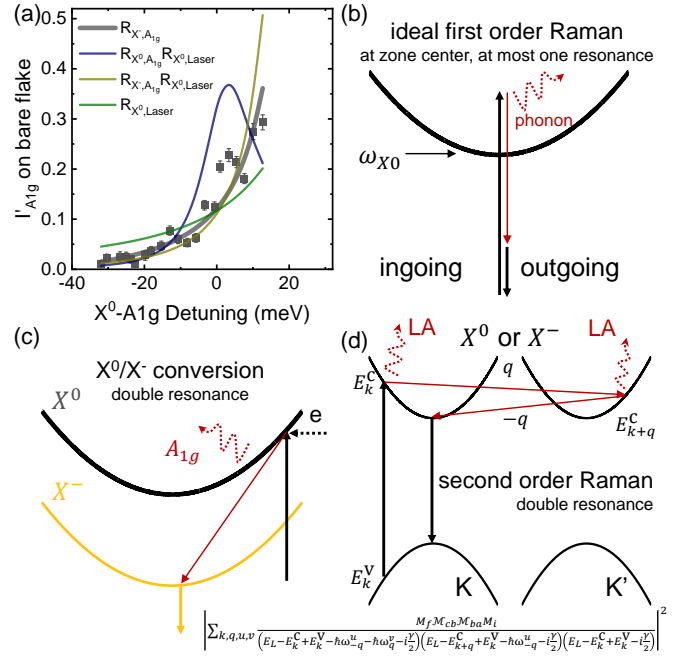
SFIG. 5. Typical beam vibrational modes.

SFIG. 6. Calculated vibrational modes for cavities with the nanobeam width d_y of 500, 400 and 300 nm. They have the similar profile and slightly different frequencies.

III. ADDITIONAL RAMAN RESULTS

A. Alternative Analysis Methods

We emphasize that the selective Raman enhancement does not rely on the quantitative fitting method and can be directly obtained from the raw data. Generally, we obtain two maximums in the Raman intensities, denoted

SFIG. 7. Analysis of raw Raman datasets without quantitative fittings. The maximum in the gray region is surely from X^0 -phonon resonance. The maximum in the yellow region surely contains contribution from X^- -phonon resonance.SFIG. 8. Schematic of Raman scatterings. (a) I'_{A1g} from the bare flake case. By comparison $R_{X^-,A1g}$ (gray line) is the best fitting. (b) The ideal first-order Raman scattering limited at zone center. (c) The phonon-assisted X^0/X^- conversion [56]. (d) The second-order 2LA scattering [30].

by the gray and yellow regions in SFIG. 7. The maximum in the gray region around zero detuning is surely from the X^0 -Raman resonance. Comparing the cavity to the control cases, the enhancement of this maximum is clearly observed. Therefore, the first conclusion of enhanced X^0 -induced Raman scattering in cavities, is obtained. One might wonder about the maximum in the yellow region. This maximum in SFIG. 7(b) surely contains the contribution from the X^- -2LA detuning, but might also be contributed by the X^0 -LA or X^0 -Laser detuning. Nonetheless, we do not need to care about how much contribution is from which detuning, because this maximum of 2LA in yellow region completely vanishes in cavities. This means all contributions vanish. Therefore, the second conclusion of suppressed X^- -induced Raman scattering in cavities, is also obtained.

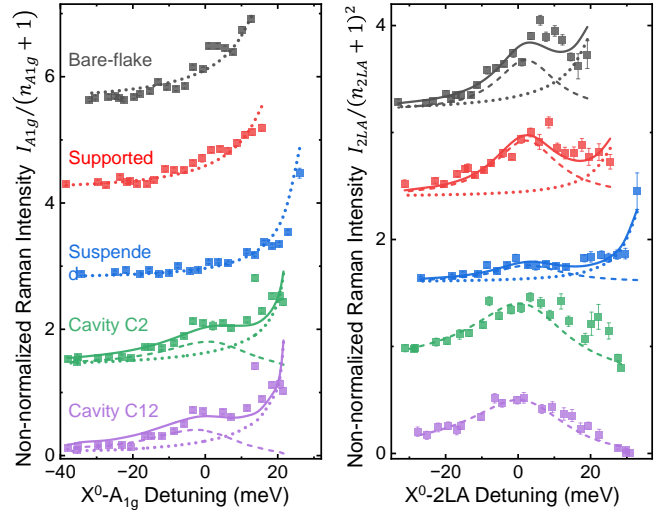
In Fig. 2(a) we use the exciton-Raman detuning $R_{X,p}$ to fit the Raman intensity since this detuning dominates the intensity variation in our measurements. Hereby, we plot the data of A_{1g} in the bare flake case in SFIG. 8(a) and discuss in detail. The gray line denotes the fitting by $R_{X^-,A1g}$ as used in the main paper. The dark blue line in SFIG. 8(a) is the prediction by $R_{X^0,A1g}R_{X^0,Laser}$ which corresponds to the ideal first-order Raman scattering schematically depicted in SFIG. 8(b). In this case, both the ingoing and outgoing section are limited at the zone center, and thereby, the Raman intensity is described by the multiple of the ingoing detuning $R_{X^0,Laser}$ and the outgoing detuning $R_{X^0,A1g}$. Obviously, SFIG. 8(b) is not

our case. Even if only considering $R_{X^0,Laser}$ (dark green line in SFig. 8(a)), the variation is much smaller than the experimental data due to the large X^0 -Laser detuning. Moreover, only considering $R_{X^0,Laser}$ is contradictory, since $R_{X^0,A1g}$ and $R_{X^0,Laser}$ are from one scattering process (SFig. 8(b)), thereby one term exists while the other term vanishes is contradictory.

The intensity of A_{1g} contains signals from the doubly resonant Raman scattering [56] depicted SFig. 8(c). In the doubly resonant scattering, the outgoing section (downward yellow arrow) is around the zone center thus follows $R_{X^-,A1g}$. In contrast, in the ingoing section (upward black arrow), the X^0 created by the laser is not at the zone center, thus does not follow $R_{X^0,Laser}$. Indeed, the ingoing section creates X^0 with the laser energy ω_{Laser} at a real energy level. Therefore, we think this probability is dominated by $1+n_{Laser}$, since excitons in the valley follows the Bose distribution with the Bose factor $n_{Laser} = 1/[e^{\hbar(\omega_{Laser}-\omega_{X0})/(k_B T)} - 1]$ [41]. In our measurements, $1+n_{Laser} \approx 1$ since $\hbar\omega_{Laser} - \hbar\omega_{X0} \gg k_B T$. Therefore, the ingoing section has little impact on the Raman intensity. As shown in SFig. 8(a), $R_{X^-,A1g}$ fits the experimental data better than $R_{X^-,A1g}R_{X^0,Laser}$ (dark yellow line).

Similarly, the intensity of 2LA contains signals from the doubly resonant Raman scattering [30] depicted in SFig. 8(d). The ingoing section is also not limited at zone center. Strictly, the Raman intensity is very complex and consists of scattering with all possible intermediate states, such as the sum equation in SFig. 8(d) reproduced from [30]. However, in our measurements the outgoing section is around resonance, thus $R_{X,p}$ plays the major role in the Raman intensity variation and is used to fit the detuning dependence. The validity of our fitting method is also supported by the comparison to the exciton-phonon coupling strength extracted from PL data as discussed later in Sec. IV A.

We normalized the intensity of A_{1g} and 2LA by the Si_3N_4 peak to remove potential noises in the measurements [10]. In addition, the normalization provides the comparison of Raman intensities between different cases. It makes no sense to compare the absolute Raman intensity between difference cases, since the laser spot size $1 \mu m$ is much larger than the nanobeam cavity width $d_y \leq 0.5 \mu m$ and d_y varies between different cavities. This means the size of MoS_2 excited by the laser varies between different cases. Nevertheless, we emphasize that our conclusions do not rely on the normalization. We present the Raman intensities of A_{1g} and 2LA without the normalization to Si_3N_4 peak in SFig. 9. As shown, the two key results are same to the normalized intensities in Fig. 2(a), including the selective enhancement of X^0 -induced scattering and the T^N dependence of the enhancement in cavities.



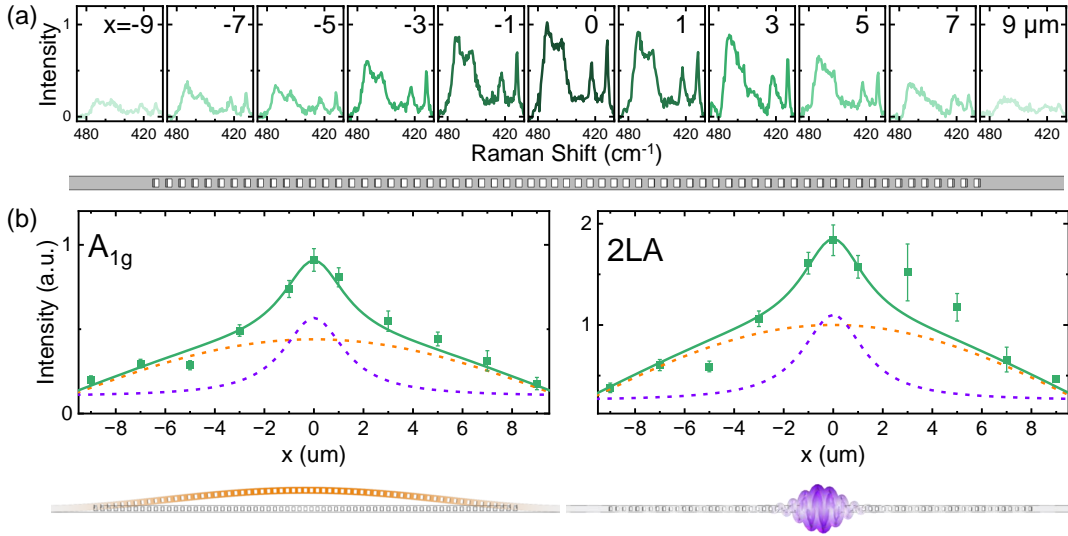
SFig. 9. Raman intensities $I_{A_{1g}}/(n_{A_{1g}} + 1)$ and $I_{2LA}/(n_{2LA} + 1)^2$ without the normalization to Si_3N_4 peak. Conclusions are same to Fig. 2 in the main paper.

B. Additional Evidence for the Coupling

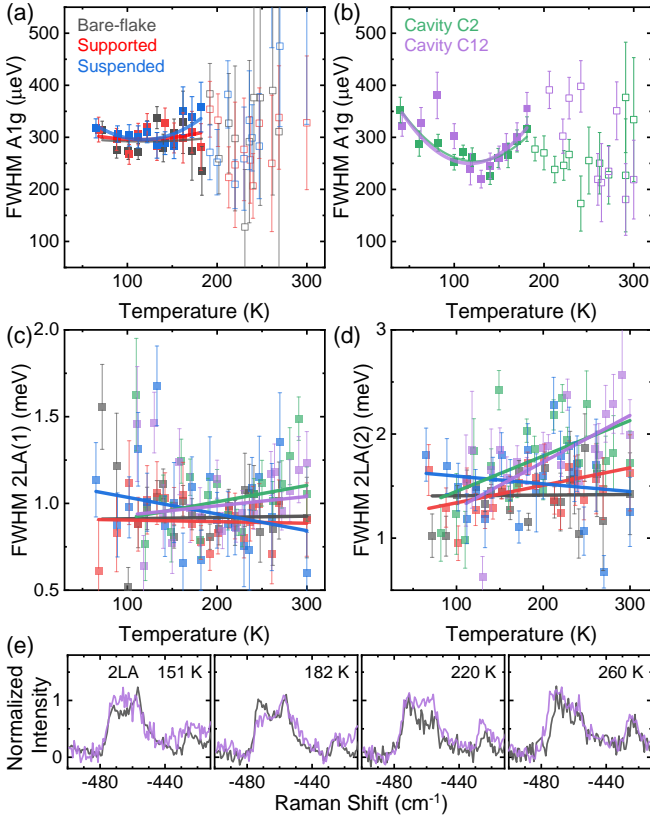
Here we present the position dependence of the Raman spectra along the nanobeam in SFig. 10(a). The Raman enhancement is generally centralized. The extracted intensity of A_{1g} and 2LA are presented in SFig. 10(b), indicating that both beam (orange) and confined (violet) vibrational modes contribute to the Raman enhancement. The beam vibrational modes have broader spatial distribution thus introduce an enhancement broad in spatial. In contrast, the confined vibrational modes introduce an enhancement narrow in spatial. The sum of two are denoted by the fitting lines in SFig. 10(b). We note that the fitting is based on the typical modes and qualitative, since there exist multiple modes for both beam (SFig. 5) and confined (SFig. 4) vibrations.

The confined vibrational modes have smaller mode volume but also smaller population (high frequency $\sim GHz$). In contrast, the beam vibrational modes have the larger population (low frequency $\sim MHz$) but larger mode volume. The exciton-phonon coupling will increase with the phonon population but decreases with the mode volume [24]. Thus, it is a reasonable result that both two types of vibrational modes contribute. We emphasize that the beam and confined vibrations are both cavity vibrational phonons. The results in SFig. 10 reveal that the tripartite coupling can occur with different kinds of nanomechanical modes, therefore, the phononic hybridization can be applied to a wide range of nanosystems.

The tripartite exciton-phonon-phonon coupling will result in an anharmonicity in Raman linewidths [62], which are indeed observed in our experiments as presented in SFig. 11. The exciton-phonon coupling introduces a temperature narrowing in the Raman linewidth whilst the phonon-phonon coupling introduces a broadening. Thus,



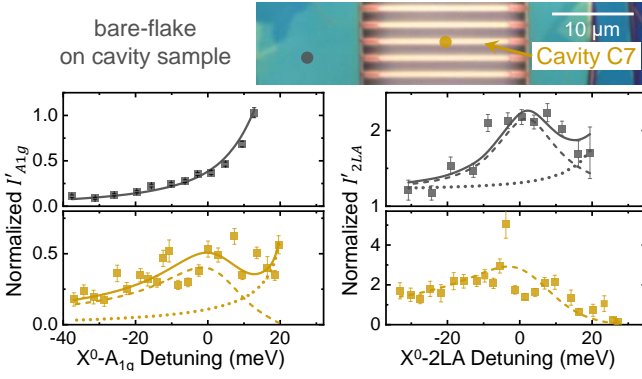
SFig. 10. Position dependence of the Raman enhancement. (a) Position-dependent Raman spectra along cavity C2, measured at $T = 268$ K. (b) Extracted Raman intensities of A_{1g} and 2LA. The position dependence indicates that both beam (orange) and confined (violet) vibrational modes contribute to the Raman enhancement.



SFig. 11. Anharmonicity in Raman linewidths. (a)(b) A_{1g} linewidth in (a) control cases and (b) cavities. Solid lines are the quadratic fittings. Hollow points are data with low SNR. (c)(d) Linewidths of two 2LA peaks (SFig. 2(b)) and the linear fittings (solid lines). (e) Raw Raman spectra normalized by the 2LA peak for comparison.

the Raman linewidth is nonmonotonic at low temperature [62]. Compared to the control cases in SFig. 11(a), we observe this nonmonotonicity in the A_{1g} linewidth in the cavities presented in SFig. 11(b). We note that for the A_{1g} linewidth in SFig. 11(a)(b), data points at high $T > 170$ K (hollow points) has huge error bar due to the low signal-to-noise ratio (SNR) of A_{1g} peak in spectra. The linewidth of two 2LA peaks extracted by the multi Lorentz fitting (SFig. 2) are presented in SFig. 11(c)(d). Since the data is a bit noisy, here we simply use a linear fitting to quantify the temperature dependence. As shown, for both two 2LA peaks the broadening in cavities are larger than that in control cases. We plot the comparison of raw data in SFig. 11(e) to show this anharmonicity straightforwardly. The anharmonicity in Raman linewidth further strengthens the tripartite coupling.

We note that the linear fitting in SFig. 11(c)(d) is a simple method to provide a quantitative comparison of the temperature dependence. The broadening of Raman linewidth from the phonon-phonon coupling can be generally expressed by a polynomial equation of the Bose factor, and the polynomial order is related to the number of phonons involved in the coupling [62]. In our sample, the Bose factor of cavity vibrational phonon is $\approx k_B T / (\hbar \omega_{cP})$ due to the low energies $\hbar \omega_{cP} \ll k_B T$ as discussed in Sec. II. Therefore, we can expect the Raman linewidth in the cavity following a polynomial equation $\sum c_j T^j$. The number of cavity vibrational phonons involved in the coupling determines j , whilst the frequency of cavity vibrational phonon is reflected in the coefficient c_j . In cavity C12 two cavity phonons are involved in the tripartite coupling (Fig. 3(a)), thereby the Raman linewidth is expected to have a quadratic temperature dependence. We have tried the quadratic fitting for the



SFig. 12. Additional Raman results to show the generality. The bare flake on the cavity sample (gray) exhibits same to the bare flake on the control experiment sample in Fig. 2. The cavity C7 (yellow) exhibits same to cavity C2 and C12.

data from cavity C12 in SFig. 11(d), but the improvement is limited by the noise. Nonetheless, the scope here is that the anharmonicity is observed and further strengthens the tripartite coupling. Specific details in the anharmonicity could be an interesting future topic.

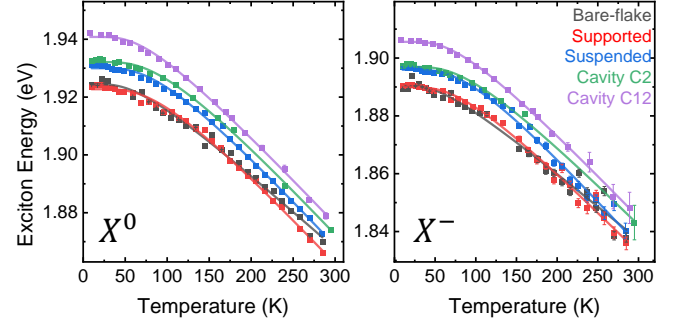
The 2D flakes for the control experiment sample and cavity sample in this work are from same bulk materials and prepared by the same methods discussed in Sec. IA. Nevertheless, one might wonder that the differences between cavities and control cases are from uncertainties during the fabrication. Here in SFig. 12 we show the Raman datasets measured from the bare flake on the cavity sample (gray) and another cavity C7 (yellow). As shown, the key results of the bare flake on the cavity sample (gray), which means the observation of X^-A_{1g} peak for A_{1g} whilst both X^0 -2LA and X^- -2LA peaks for 2LA, are same to the bare flake on the control experiment sample in Fig. 2. The key results of cavity C7 (yellow) are also same to those of C2 and C12, which means the observation of both X^-A_{1g} and X^0A_{1g} peaks for A_{1g} whilst only X^0 -2LA peak for 2LA. These results exclude the uncertainties during the sample fabrication. In addition, the enhancement of $g_{X^0,2LA}$ in cavity C7 exhibits a T^3 dependence ($N = 2.79 \pm 0.47$) that further strengthens a discrete number of cavity phonons participate in the tripartite exciton-phonon-phonon coupling.

IV. PL SPECTROSCOPY

A. Selective Exciton-Cavity-Phonon Coupling

We present the emission peak energies of X^0 and X^- extracted from PL spectroscopy in SFig. 13. The exciton energy in TMDs usually follows the standard hyperbolic cotangent relation [25] as

$$\omega_X = \omega_0 - S\langle\hbar\omega\rangle_E \left[\coth\left(\frac{\langle\hbar\omega\rangle_E}{k_B T}\right) - 1 \right] \quad (1)$$



SFig. 13. Temperature-dependent energy shift of X^0 and X^- in five cases. All follow the standard relation.

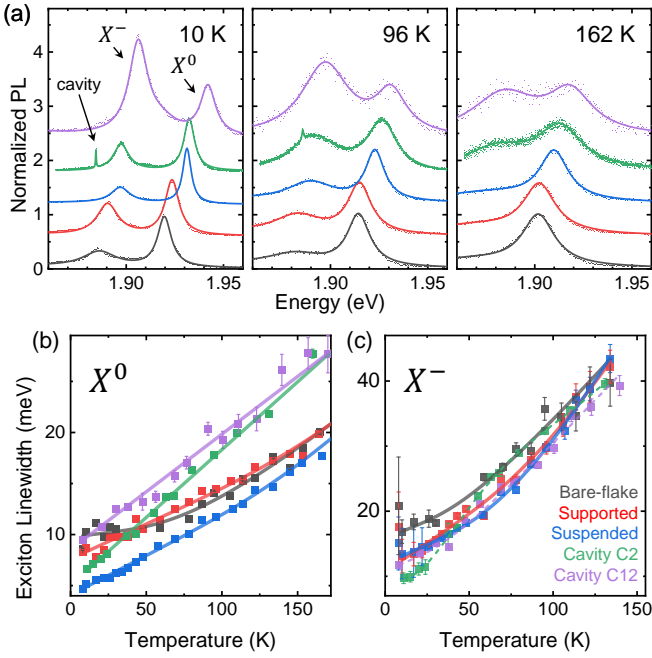
where ω_0 is the exciton energy at zero temperature, S is a dimensionless coupling constant, $\langle\hbar\omega\rangle_E$ is an average phonon energy and k_B is the Boltzmann constant. In both control cases and cavities, both the X^0 and X^- energy is well described by Eq. (1). For X^0 in the bare flake, supported, suspended, cavity C2 and cavity C12 cases, we observe $S = 1.52 \pm 0.06$, 1.87 ± 0.06 , 1.89 ± 0.04 , 1.88 ± 0.06 , 1.82 ± 0.04 and $\langle\hbar\omega\rangle_E = 16 \pm 2$, 23 ± 1 , 22 ± 1 , 24 ± 1 , 18 ± 1 meV, respectively. For X^- , we observe $S = 1.37 \pm 0.10$, 1.69 ± 0.08 , 1.88 ± 0.08 , 1.68 ± 0.07 , 1.75 ± 0.04 and $\langle\hbar\omega\rangle_E = 14 \pm 3$, 21 ± 2 , 23 ± 2 , 22 ± 2 , 19 ± 1 meV respectively. Little difference is observed between the five cases, and all fitting parameters agree well to previous reports [25].

As discussed in the main paper, since in Raman spectra (excited by 632 nm-laser) the exciton emission line shape is strongly deformed by the phonon couplings [29], exciton emission properties directly extracted from Raman spectra might be inaccurate. Therefore, we calculate the exciton emission properties in Raman spectra by the PL data presented here. We use Eq. (1), with S and $\langle\hbar\omega\rangle_E$ extracted from SFig. 13, in addition with an ω'_0 aligned by the X^0 -Raman resonant T point, to calculate the X^0 and X^- energies in the Raman analyses. We have to align ω'_0 since the different measurement setups for PL and Raman spectroscopy introduce inaccuracy in the absolute value of photon energies in the spectra. The X^0 and X^- linewidths are calculated by the fitting curves in SFig. 16 discussed later.

We present the emission peak linewidth of X^0 and X^- at low temperature $T < 175$ K in SFig. 14. Typical PL spectra recorded from five cases around 10, 96 and 162 K are presented in SFig. 14(a) for comparison. The exciton linewidths at low T are nearly same in five cases. However, as T increases, the X^0 linewidth in the cavities exhibits a significant broadening compared to that in control cases. This broadening indicates the exciton-phonon coupling is modulated in the cavities.

The exciton linewidth in 2D semiconductors usually follows the phenomenological equation [15, 16, 25]

$$\gamma = \gamma_0 + a_1 T + \frac{a_2}{\exp\left(\frac{\langle\hbar\omega\rangle_L}{k_B T}\right) - 1} \quad (2)$$



SFig. 14. (a) Typical PL spectra recorded from five cases around 10, 96 and 162 K. The sharp peak in cavity C2 at 10 K is from the photonic mode. (b) Temperature-dependent exciton linewidth of X^0 and (c) X^- in five cases.

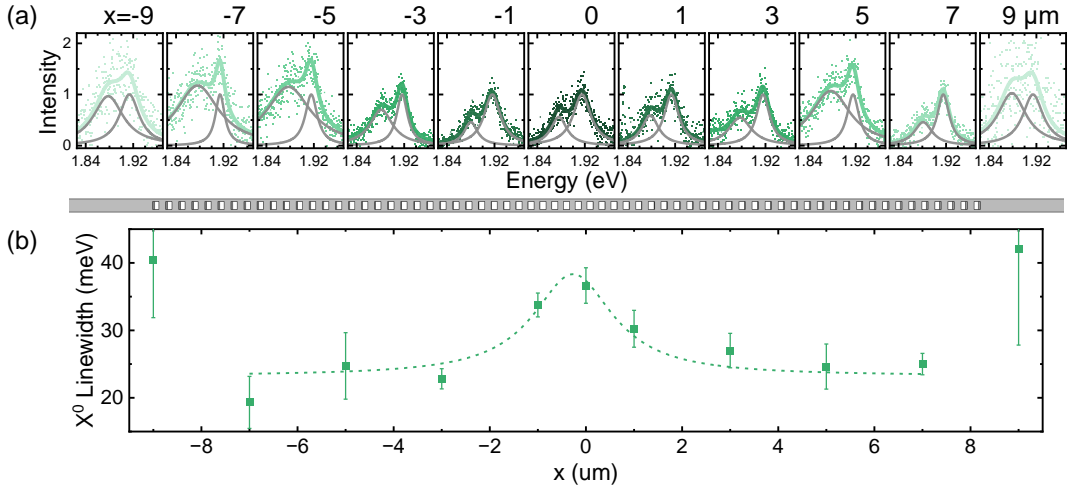
where γ_0 is the intrinsic X^0 or X^- linewidth, a_1 (slope at low T) quantifies the strength of linear T -broadening induced by low-energy acoustic phonons and a_2 is the nonlinear broadening arising from high-energy phonons with an average energy $\langle \hbar\omega \rangle_L$. Measured linewidths of X^0 (γ_{X^0}) and X^- (γ_{X^-}) are presented in SFig. 14(b)(c) respectively. For γ_{X^0} in SFig. 14(b), the three control cases (gray, red, blue) are well described by Eq. (2). The fitting terms in the bare flake case (gray) quantitatively agree with previous reports, including the coupling strengths $a_{1,X^0} = 18.5 \pm 1.7 \mu\text{eV} \cdot \text{K}^{-1}$ and $a_{2,X^0} = 29.8 \pm 5.8 \text{ meV}$ [15, 16, 25]. In the supported (red) and suspended (blue) cases, local static strain from the Si_3N_4 and the suspension is induced as discussed in the main paper. The best fit values $a_{1,X^0} = 68.5 \pm 4.9$ (77.5 ± 3.2) $\mu\text{eV} \cdot \text{K}^{-1}$ and $a_{2,X^0} = 91 \pm 48$ (77 ± 20) meV for the supported (suspended) case are larger than those in the bare flake, consistent with strain-induced cases reported previously [42–44]. In contrast to three control cases, γ_{X^0} recorded from the cavities behaves quite differently. Specifically, we observe a linear T -broadening up to 150 K, with the slope $a_{1,X^0} = 133 \pm 2$ (113 ± 4) $\mu\text{eV} \cdot \text{K}^{-1}$ in cavity C2 (C12), almost double the value obtained in the control cases. This enhanced value of a_{1,X^0} indicates that the coupling between X^0 and low-energy phonons in the cavity is stronger compared to the control cases, unveiling the contribution from cavity vibrational phonons. The cavity phonons exactly have low energies $\ll k_B T$ as discussed in Sec. IA thereby contributes to the linear broadening [15, 25].

In contrast to X^0 , the X^- linewidth shows little difference between the four cases as presented in SFig. 14(c). The inaccuracy of γ_{X^-} at low T is mainly from the fine structure of MoS_2 trions [39] shown in SFig. 3(b). Despite this, γ_{X^-} is well described by Eq. (2) for the three control experiments (gray, red, blue), and the linear term a_{1,X^-} is 106 ± 31 , 154 ± 20 , $114 \pm 8 \mu\text{eV} \cdot \text{K}^{-1}$, respectively. Although γ_{X^-} in cavities (green, purple) cannot be appropriately described by Eq. (2), no additional broadening beyond the control cases is observed. Based on the PL linewidths in SFig. 14, we conclude that the X^0 -cavity-phonon coupling strength is much stronger than the X^- -cavity-phonon coupling strength. This selectivity in the bipartite coupling between excitons and cavity phonons perfectly agrees with the selectivity in the tripartite coupling. Similar phenomena that different excitons couple to different phonons have also been observed in other semiconductors [45].

In addition, the coupling strength a_{1,X^0} and a_{1,X^-} extracted from PL spectra provide a comparison to the coupling strength $g_{X^0,2\text{LA}}$ and $g_{X^-,2\text{LA}}$ in the fitting of Raman spectra $I'_{2\text{LA}} = g_{X^0,2\text{LA}} R_{X^0,2\text{LA}} + g_{X^-,2\text{LA}} R_{X^-,2\text{LA}}$ presented in Fig. 2(a). The ratio $a_{1,X^-}/a_{1,X^0}$ is 5.7 ± 2.2 , 2.2 ± 0.5 , 1.5 ± 0.2 for the bare flake, supported and suspended case, respectively. The ratio $g_{X^0,2\text{LA}}/g_{X^-,2\text{LA}}$ in the three control cases 5.1 ± 1.6 , 2.0 ± 0.6 , 2.0 ± 0.4 generally agree to those observed from the PL spectra. This agreement further supports our fitting method discussed for SFig. 8.

To further strengthen the X^0 -cavity-phonon coupling, we record the position-dependent PL spectra along cavity C2, as presented in SFig. 15(a). The X^0 linewidth γ_{X^0} is presented in SFig. 15(b). As expected, γ_{X^0} exhibits a centralized broadening due to the cavity vibrational modes are centralized (SFig. 10), further supporting the X^0 -cavity-phonon coupling discussed in SFig. 14. These agreements between Raman and PL spectroscopy, including the selectivity to X^0 (Fig. 2 and SFig. 14) and the position dependence (SFig. 10 and SFig. 15), further strengthens the conclusions of phononic hybridization.

In contrast to the position dependence of Raman enhancement presented in SFig. 10(b), the position dependence in PL linewidth is less clear, e.g., we cannot distinguish the contributions from beam and confined modes in SFig. 15(b). The worse distinguishability in PL datasets compared to Raman datasets is since that Raman spectroscopy is the direct measurement of phonons. In contrast, PL spectroscopy is an indirect measurement i.e., Eq. (2) shows that the exciton-phonon coupling is reflected by the T -broadening rather not absolute value of exciton linewidth. Besides the exciton-phonon coupling, there exist other factors affecting the exciton linewidth such as the quality of TMD (commercial or grown) [25]. As a result, usually γ_{X^0} is slightly different in different cases, which is clearly shown in SFig. 14. Nonetheless, the position dependence of γ_{X^0} in SFig. 15 clearly exhibits the centralized broadening, indicating the exciton-phonon coupling dominates the exciton linewidth as the



SFig. 15. Position dependence of X^0 linewidth broadening. (a) Position-dependent PL spectra of cavity C2 measured at 170 K, normalized by X^0 peak at 1.91 eV. (b) Extracted X^0 linewidth along the nanobeam, exhibiting a centralized broadening.

temperature increases.

B. Phonon-Phonon Nonlinearity

In Sec. IV A we mainly focus on the exciton linewidth at low temperature below 175 K. Before presenting the PL data at high temperature, we first discuss the limitation of PL datasets.

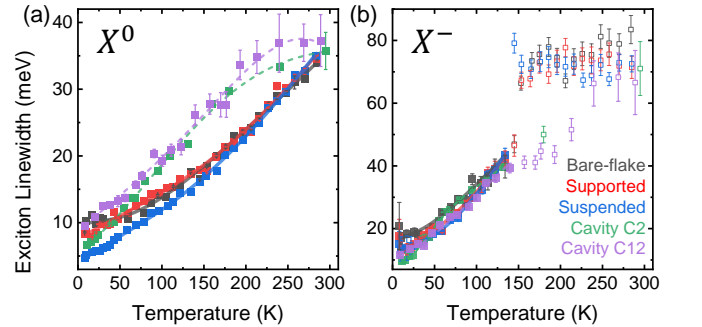
In SFig. 14, we use phenomenological equation Eq. (2) to fit the exciton linewidth in control cases (gray, red, blue) and use the linear broadening $\gamma = \gamma_0 + a_1 T$ to fit the X^0 linewidth below 175 K in the cavities. The linear term $a_1 T$ has the clear physical meaning – coupling to low-energy phonons – because for phonon with low energy $\hbar\omega$, the Bose factor $\approx k_B T / (\hbar\omega) \propto T$ as discussed in Sec. II, and the corresponding broadening of exciton linewidth is also $\propto T$ [15]. Thus, the broadening from different low-energy phonons can be summed linearly, and the sum is still proportional to T such as

$$c_1 \frac{k_B T}{\hbar\omega_1} + c_2 \frac{k_B T}{\hbar\omega_2} = \langle c \rangle \frac{k_B T}{\langle \hbar\omega \rangle} \quad (3)$$

where c_1 , c_2 reflects the exciton-phonon coupling with a single phonon and $\langle c \rangle$, $\langle \hbar\omega \rangle$ reflects the average effect of two phonons $\hbar\omega_1$ and $\hbar\omega_2$. However, the nonlinear term in Eq. (2) is a phenomenological term with the Bose factor of “average” phonon energy $\langle \hbar\omega \rangle_L$. But for high-energy phonons, their Bose factor is not proportional to T . The sum of Bose factors of two high-energy phonons cannot be described by a new Bose factor as

$$\frac{c_1}{\exp\left(\frac{\hbar\omega_1}{k_B T}\right) - 1} + \frac{c_2}{\exp\left(\frac{\hbar\omega_2}{k_B T}\right) - 1} \neq \frac{\langle c \rangle}{\exp\left(\frac{\langle \hbar\omega \rangle}{k_B T}\right) - 1} \quad (4)$$

. Thus, the exciton linewidth broadening from different high-energy phonons cannot be simply averaged, and the



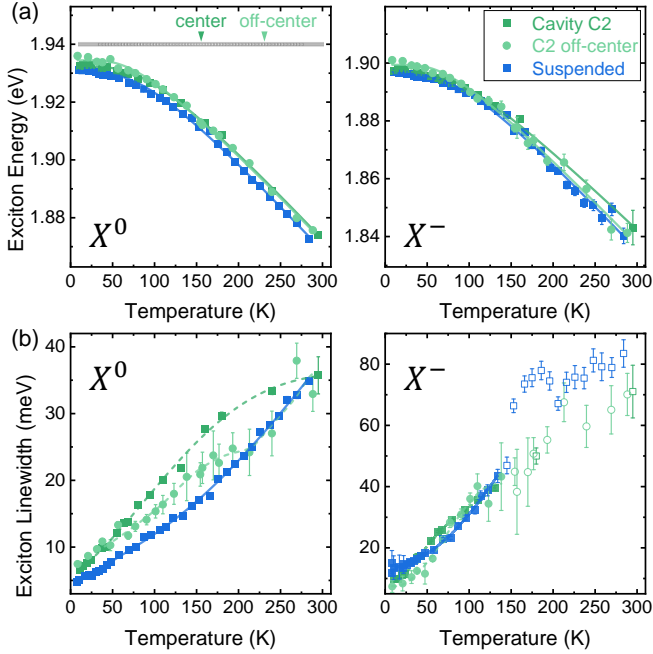
SFig. 16. Temperature-dependent linewidth of (a) X^0 and (b) X^- in five cases. The hollow points in (b) is inaccurate due to the merge of X^- and D^- peak shown in SFig. 3(b).

nonlinear term in Eq. (2) is not strictly correct. This is the reason why in Sec. IV A we mainly focus on PL data below 175 K, where the linear exciton linewidth broadening has direct physical meanings (coupling with low-energy phonons).

Nonetheless, here we try to provide an explanation of the non-trivial exciton linewidth at high temperature. We present the X^0 and X^- linewidth at all temperature points in SFig. 16(a)(b), respectively. In the two cavities (green, purple), the X^0 linewidth γ_{X^0} in the whole measurement range $T \in (0, 300)$ K cannot be described by Eq. (2), thus is fitted by a polynomial equation

$$\gamma_{X^0} = \gamma_0 + c_1 T + c_2 T^2 + c_3 T^3 + c_4 T^4 \quad (5)$$

shown by the dashed lines in SFig. 3(a). We use Eq. (5) just to sketch a fitting to estimate the value of γ_{X^0} at other T points. The nonlinear parameters c_i ($i \geq 2$) have no general physical meanings as discussed in Eq. (4). Generally, γ_{X^0} exhibits similar behavior in both two cavities: approximately a linear T -broadening below 175 K whilst the T -broadening rate saturates above 175 K. The



SFig. 17. Temperature-dependent (a) exciton energies (b) linewidths measured at cavity C2 off-center (light green dots), $\sim 5 \mu\text{m}$ away from the nanobeam center position. Datasets of cavity C2 center (green rectangles) and suspended case (blue rectangles) from SFig. 13 and SFig. 16 are also plotted here for comparison.

non-trivial γ_{X^0} at high temperature $T > 175 \text{ K}$ further indicates the nonlinear term in Eq. (2) is not suitable for all cases.

The X^- linewidth γ_{X^-} at high temperature $T > 150 \text{ K}$ (hollow points in SFig. 16(b)) is inaccurate due to the overlap between X^- and D^- peak as discussed in SFig. 3(b). Moreover, around 150 K where γ_{X^0} exhibits maximum difference between cavities and control cases, γ_{X^-} exhibits little difference between five cases. Thereby, the conclusion of weak X^- -cavity-phonon coupling is same to that obtained from Raman spectra. Similar to γ_{X^0} , we fit γ_{X^-} in two cavities by Eq. (5) just to sketch a fitting to estimate the value of γ_{X^-} at other T points.

To further investigate the interplay between the non-trivial γ_{X^0} and the cavity vibrational phonons, we next discuss the position dependence of γ_{X^0} since the cavity phonons are position-dependent as discussed in SFig. 10 and SFig. 15. The absolute value of γ_{X^0} in SFig. 15 is not a strict reflection of the exciton-phonon coupling. Therefore, we measure the temperature dependent PL spectra at an off-center position in cavity C2, which is $\sim 5 \mu\text{m}$ away from the nanobeam center. We present the extracted exciton energies and linewidths (light green dots) in SFig. 17, along with the results from cavity C2 center (green rectangles) and the suspended case (blue rectangles) for comparison. For the exciton energies in the off-center case (SFig. 17(a)), we observe

$S = 1.83 \pm 0.05$, $\langle \hbar\omega \rangle_E = 20 \pm 1 \text{ meV}$ for X^0 and $S = 1.78 \pm 0.08$, $\langle \hbar\omega \rangle_E = 19 \pm 2 \text{ meV}$ for X^- . These values are same to those observed in other cases (SFig. 13) and in previous works [25], thereby further strengthen the conclusion that the exciton energies are rarely affected by the cavity vibrational phonons.

The exciton linewidths in the off-center case presented in SFig. 17(b) generally exhibit similar behavior to those at center. Same to SFig. 14(c) and SFig. 16(b), the X^- linewidth γ_{X^-} exhibits little difference between the center, off-center and control cases. This agreement further strengthens the weak X^- -cavity-phonon coupling. As T increases, the X^0 linewidth γ_{X^0} in the off-center case firstly behavior like that at center: approximately a linear T -broadening below 120 K and then a saturation over 120 K. However, after being “caught up” by the suspended case at 210 K, the T -broadening rate of γ_{X^0} in the off-center case again increases. At $T > 210 \text{ K}$, γ_{X^0} in the off-center case approximately follows the suspended case. Generally, the off-center case behavior like a “medium” between the cavity center and the control case. The “medium” is reasonable, since the off-center case has part of the cavity vibrational phonons (beam modes) but not all (no confined modes) as discussed in SFig. 10.

Finally, we try to explain the non-trivial X^0 linewidth at high temperature. One possible reason is the non-linearity in mechanics, i.e., nonlinearity in the Young’s moduli and deformation potentials [46, 47]. The mechanics discussed up to now is in linear regime which means the deformation-induced strain and electron (hole) potential change are all proportional to the deformation. In this linear regime, the vibration amplitude (cavity phonon population) does not affect the phononic mode (frequency and Q factor). Generally, the mechanics is linear with small deformations but nonlinear with large deformations. E.g., as the cavity vibration amplitude (phonon population) increases with T , we could image above some points the strain increases superlinearly to the deformation, thus the vibration saturates. However, the nonlinearity in cavity vibration is usually observed with strong external driving such as a piezo with huge AC voltage [48]. The natural thermal excited vibrations usually have small deformations within the linear regime. Thereby, we think the nonlinearity in mechanics is improbable.

As such, we suggest the saturation in T -broadening is not due to the nonlinearity of mechanics, but rather due to the nonlinearity in the broadening effects of the phonon couplings. Usually, the decay rate (linewidth) of an exciton γ_X is written as

$$\gamma_X = \gamma_{rad} + \gamma_{non-rad} \quad (6)$$

where γ_{rad} is the radiative decay rate and $\gamma_{non-rad}$ is the non-radiative decay and dephasing rate written as

$$\gamma_{non-rad} = \sum_i \gamma_{phi} + \gamma_{others} \quad (7)$$

where $\gamma_{phi, i} = 1, 2, \dots$ means the exciton-phonon coupling to phonon ph1, ph2, \dots and γ_{others} describes other non-radiative decay channels. We emphasize that here the decay rate $\gamma_{rad}, \gamma_{ph1}, \gamma_{ph2}, \dots$ and γ_{others} are summed linearly. This linear sum means these decay channels are independent to each other. The independence is usually valid, e.g., the phonon-phonon coupling between different lattice phonons is usually very weak, thus $\gamma_{ph1} + \gamma_{ph2}$ is reasonable when ph1 and ph2 are both lattice phonons.

However, the cavity phonon is not independent to the lattice phonon. We observe the lattice-phonon—cavity-phonon coupling, and such coupling increases with temperature T . Therefore, we could expect that the sum of γ_{cavity} (broadening from cavity phonons) and $\gamma_{lattice}$ (broadening from lattice phonons) is approximately linear (independent) at low T as $\gamma_{cavity} + \gamma_{lattice}$ but non-linear (correlated) at high T such as

$$(\gamma_{cavity}^k + \gamma_{lattice}^k)^{1/k} \quad (8)$$

where k is a dimensionless quantitation of the phonon-phonon nonlinearity (coupling) increasing with T . Therefore, at high T the phonon-induced linewidth broadening is smaller than $\gamma_{cavity} + \gamma_{lattice}$, resulting in the saturation we observed in experiments.

Based on this nonlinearity between cavity and lattice phonons, we propose a phenomenological model to explain X^0 linewidth. The lattice-phonon-induced broadening is written as

$$\gamma_{lattice} = a_1 T + \frac{a_2}{\exp\left(\frac{\langle \hbar \omega \rangle_L}{k_B T}\right) - 1} \quad (9)$$

following the Eq. (2). The cavity-phonon-induced broadening is written as

$$\gamma_{cavity} = c_1 T \quad (10)$$

since the cavity phonons have low energies as discussed in Sec. IA. The phonon-induced broadening is then calculated by Eq. (8) as

$$\gamma_{phonon} = (\gamma_{cavity}^k + \gamma_{lattice}^k)^{1/k} \quad (11)$$

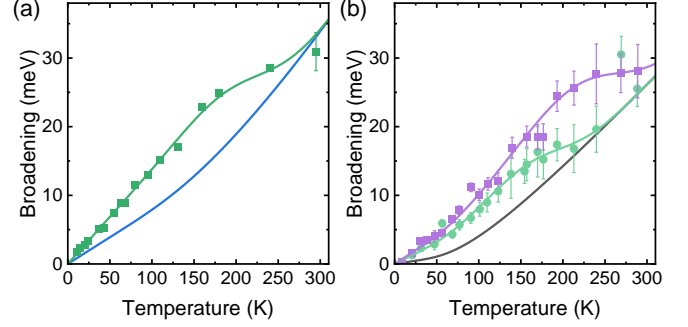
. We set k which describes the phonon-phonon nonlinearity (coupling) as

$$k = 1 + \left(\frac{T}{T_0}\right)^m \quad (12)$$

where T_0 describes the saturation temperature and m is a dimensionless parameter.

We present the fitting of cavity C2 based on Eq. (11) in SFig. 18(a). The intrinsic X^0 linewidth γ_0 at zero temperature is 5.0 ± 0.1 meV in cavity C2, close to that value in the suspended case 4.1 ± 0.2 meV. Thereby, we use $\gamma_{lattice}$ extracted from the suspended case (blue line)

for the fitting, including $a_{1, X^0} = 77.5 \pm 3.2 \mu\text{eV} \cdot \text{K}^{-1}$, $a_{2, X^0} = 77 \pm 20$ meV and $\langle \hbar \omega \rangle_L = 54.6 \pm 6.8$ meV. The



SFig. 18. Fitting of non-trivial X^0 linewidth based on the nonlinearity between lattice and cavity phonons. (a) Cavity C2 (green) based on $\gamma_{lattice}$ from the suspended case (blue). (b) Cavity C2 off-center (light green) and cavity C12 (purple) based on $\gamma_{lattice}$ from the bare flake (gray).

green line in SFig. 18(a) is the fitting calculated with $c_1 = 60 \pm 3 \mu\text{eV}/\text{K}$ for γ_{cavity} , $T_0 = 238 \pm 9$ K and $m = 6$. In contrast, γ_0 in cavity C2 off-center and cavity C12 is 6.9 ± 0.4 and 8.5 ± 0.2 meV respectively, close to that value in the bare flake case 9.7 ± 0.4 meV. Thereby, we fit these two cases based on $\gamma_{lattice}$ extracted from the bare flake case (gray line) as presented in SFig. 18(b). Parameters for $\gamma_{lattice}$ are $a_{1, X^0} = 18.5 \pm 1.7 \mu\text{eV} \cdot \text{K}^{-1}$, $a_{2, X^0} = 29.8 \pm 5.8$ meV and $\langle \hbar \omega \rangle_L = 23.1 \pm 5.8$ meV. The cavity C2 off-center position (light green line) is fitted with $c_1 = 43 \pm 3 \mu\text{eV}/\text{K}$, $T_0 = 205 \pm 8$ K and $m = 6$. The cavity C12 (purple line) is fitted with $c_1 = 61 \pm 2 \mu\text{eV}/\text{K}$, $T_0 = 270 \pm 6$ K and $m = 7$. As presented in SFig. 18, the fittings quantitatively agree with the experimental results. The X^0 -cavity-phonon coupling term c_1 is smaller at the off-center position compared to the values at two cavity centers, consistent to the discussions in SFig. 10, SFig. 15 and SFig. 17. The saturation temperature T_0 is also smaller at the off-center position. We explain this by the larger population of the beam vibrational phonons off-center (MHz) compared to the confined vibrational phonons at center (GHz). Therefore, the population required for the nonlinearity corresponds to lower T_0 for the beam vibrational phonons (off-center) and higher T_0 for the confined vibrational phonons (at center).

We emphasize that the exciton linewidth at high temperature is non-trivial and not deeply studied yet. We propose the model of Eqs. (10)-(12) to provide a phenomenological explanation of our experimental observations. The fitting results in SFig. 18 show that the nonlinearity between cavity and lattice phonons described in our model can quantitatively reproduce the experimental results, but we cannot exclude all other possibilities. Nonetheless, the non-trivial X^0 linewidth at high temperature discussed here affect neither our conclusions in the main paper based on Raman spectra, nor the conclusions in Sec. IV A based on low-temperature PL data.